JCB Journal of Cell Biology

TOOLS

Tunable DNMT1 degradation reveals DNMT1/DNMT3B synergy in DNA methylation and genome organization

Andrea Scelfo[1], Viviana Barra[1,2*], Nezar Abdennur[3,4,5*], George Spracklin[4,5*], Florence Busato[6], Catalina Salinas-Luypaert[1], Elena Bonaiti[1], Guillaume Velasco[7], Frédéric Bonhomme[8], Anna Chipont[9], Andréa E. Tijhuis[10], Diana C.J. Spierings[10], Coralie Guérin[9,11], Paola Arimondo[8], Claire Francastel[7], Floris Foijer[10], Jörg Tost[6], Leonid Mirny[5,12], and Daniele Fachinetti[1]

DNA methylation (DNAme) is a key epigenetic mark that regulates critical biological processes maintaining overall genome stability. Given its pleiotropic function, studies of DNAme dynamics are crucial, but currently available tools to interfere with DNAme have limitations and major cytotoxic side effects. Here, we present cell models that allow inducible and reversible DNAme modulation through DNMT1 depletion. By dynamically assessing whole genome and locus-specific effects of induced passive demethylation through cell divisions, we reveal a cooperative activity between DNMT1 and DNMT3B, but not of DNMT3A, to maintain and control DNAme. We show that gradual loss of DNAme is accompanied by progressive and reversible changes in heterochromatin, compartmentalization, and peripheral localization. DNA methylation loss coincides with a gradual reduction of cell fitness due to G1 arrest, with minor levels of mitotic failure. Altogether, this system allows DNMTs and DNA methylation studies with fine temporal resolution, which may help to reveal the etiologic link between DNAme dysfunction and human disease.

Introduction

Epigenetic modifications are master regulators of chromatin dynamics. They influence the association to DNA and downstream functions of binding factors, ultimately leading to tight control of various biological processes such as gene expression and chromatin conformation. The fundamental role of epigenetic information is highlighted by the fact that it is heritable over cell divisions.

DNA methylation (DNAme) was the first epigenetic modification described in mammals (Hotchkiss, 1948). It is accomplished by the covalent binding of a methyl moiety transferred from *S*-adenosyl-*L*-methionine to the fifth carbon of cytosine in the context of CpG dinucleotides. This enzymatic reaction generates 5-methylcytosine (5mC). 5mC, which accounts for 4% of all cytosines (Breiling and Lyko, 2015), is frequently referred to as "the fifth base"; typically, 80% of CpGs in mammalian genomes are methylated. Nevertheless, about 60% of mammalian genes have promoters with high CpG density normally devoid of methylation, called CpG islands (CGIs) (Bird, 1986). Methylated promoter CGIs also exist: it is the case of long-term repressed genes, such as germline and imprinted genes (Jones, 2012). Somatic DNAme domains are erased during primordial germ cells (PGCs) formation and in early embryos to establish a totipotent germline epigenotype and deposited de novo during early development. DNAme patterns undergo massive reshaping during differentiation, lineage specification, and in response to external cues. Once established, they are maintained and inherited throughout cell divisions (Razin and Shemer, 1995). DNAme plays an important role in genome stability by keeping silent the expression and transposition activity of repetitive DNA elements (Slotkin and Martienssen, 2007). De novo

[1]Institut Curie, PSL Research University, Sorbonne Université, CNRS, UMR 144, Paris, France; [2]Department of Biological, Chemical and Pharmaceutical Sciences and Technologies, University of Palermo, Palermo, Italy; [3]Program in Bioinformatics and Integrative Biology, UMass Chan Medical School, Worcester, MA, USA; [4]Department of Systems Biology, UMass Chan Medical School, Worcester, MA, USA; [5]Institute for Medical Engineering and Sciences, Massachusetts Institute of Technology, Cambridge, MA, USA; [6]Centre National de Recherche en Génomique Humaine, CEA-Institut de Biologie François Jacob, Université Paris-Saclay, Evry, France; [7]Université de Paris Cité, CNRS UMR 7216, Paris, France; [8]Epigenetic Chemical Biology, Institut Pasteur, CNRS UMR n°3523 Chem4Life, Université Paris Cité, Paris, France; [9]Cytometry Platform, Institut Curie, Paris, France; [10]European Research Institute for the Biology of Ageing, University Groningen, University Medical Center Groningen, Groningen, Netherlands; [11]Université Paris Cité, INSERM, Paris, France; [12]Department of Physics, Massachusetts Institute of Technology, Cambridge, MA, USA.

*V. Barra, N. Abdennur, and G. Spracklin contributed equally to this paper. Correspondence to Daniele Fachinetti: daniele.fachinetti@curie.fr; Andrea Scelfo: andrea.scelfo@curie.fr.

deposition of methyl groups is catalyzed by DNA methyltransferases (DNMT) 3A, 3B (and 3C in mouse) and maintained by DNMT1 (Chen and Riggs, 2011). However, these distinct enzymatic functions are not strictly divided among DNMTs, as DNMT3A and 3B may also be necessary for the preservation of already-established methylation patterns (Liang et al., 2002; Walton et al., 2011), and DNMT1 can methylate de novo in certain conditions, like at transposable elements, and in cancer (Arand et al., 2012; Fatemi et al., 2002; Haggerty et al., 2021; Jair et al., 2006). However, whether this is accomplished directly by DNMT1 or by interacting partners is still debated (Hervouet et al., 2018).

Like other epigenetic modifications, DNAme is a reversible process. Two main demethylating pathways have been proposed: active and passive. The active DNA demethylation pathway involves the iterative oxidation of 5mC by TET (ten eleven translocation) enzymes, which leads to the formation of 5-carboxylcytosine (5caC) (Ito et al., 2011). 5caC is the substrate for thymidine DNA glycosylase–mediated base excision repair, ultimately leading to unmodified cytosine (Shen et al., 2013). Another proposed pathway of active demethylation relies on the deamination activity of 5mC by the AID/APOBEC family members (Schutsky et al., 2017). In contrast, passive loss of DNAme does not rely on any enzymatic activity; rather, it is caused by dilution of 5mC through rounds of DNA replication in the absence of maintenance activity.

DNAme is essential for vertebrate physiology as it regulates, directly or indirectly, different genome functions, such as gene expression, silencing of transposons, chromatin condensation, imprinting and the inactivation of the X chromosome, overall maintenance of genome stability (Greenberg and Bourc'his, 2019), and correct development (Bestor et al., 2015). Severe pathologies and genetic syndromes are associated with altered functions of DNMTs (Samanta et al., 2017); for example, mutations in *DNMT3B* cause immunodeficiency, centromeric instability, and facial anomalies syndrome, a rare developmental disease (Hansen et al., 1999), and alterations of imprinted DNAme patterns during development cause Prader–Willy and Angelman syndromes (Robertson, 2005). Furthermore, aberrant DNAme domains were the first epigenetic anomalies observed in human cancer (Feinberg and Vogelstein, 1983), where hypermethylation of the promoters of specific tumor suppressor genes is associated with transcriptional silencing, while repetitive sequences are massively hypomethylated (Nishiyama and Nakanishi, 2021).

The major function of DNAme is to regulate transcription by acting on gene promoters and gene bodies and/or by influencing the formation and maintenance of heterochromatin domains, which are mainly marked by H3K9me3 (Meissner et al., 2008). In addition, the presence of histone tail modifications can shape genomic DNAme patterns by controlling the recruitment of DNMTs to the DNA (Fu et al., 2020). DNAme can contribute to the establishment of chromatin states by influencing the binding of transcriptional regulators to gene promoters and the function of chromatin remodelers (Jin et al., 2011). DNAme may play a key role in genome organization as perturbing DNMTs' activity drastically remodels chromosome compartmentalization (Du et al., 2021; Spracklin et al., 2023), and DNAme enhances chromatin compaction and stiffness in in vitro studies (Choy et al., 2010). DNAme also impacts nucleosome positioning and the mechanical and physical properties of DNA (Carollo and Barra, 2023). However, due to the complexity of genome organization and histone modification patterns, how DNAme affects chromatin organization over time is still unknown.

DNMT1 is necessary for long-term cell survival and its depletion results in severe mitotic defects (Chen et al., 2007). However, DNMT knock-down/out experiments have resulted in either inefficient protein depletion or the generation of smaller isoforms retaining methylation activity (Egger et al., 2006; Rhee et al., 2000; Spada et al., 2007). Consequently, such systems have been unable to fully elucidate the roles of DNMT1 and DNAme maintenance and lack temporal detail. As an alternative, demethylating agents (DNMTs inhibitors such as 5-azacytidine and 2′deoxy-5-azacytidine [DAC]) have been used to investigate DNAme, but these cause unavoidable secondary cytotoxic effects (Jüttermann et al., 1994). Alternative strategies achieved targeted demethylation using a fusion of the TET enzyme and inactive Cas9 (dCas9) (Choudhury et al., 2016; Liu et al., 2016) or exploiting the steric hindrance created by dCas9 on the DNA preventing DNMT binding (Sapozhnikov and Szyf, 2021). However, these approaches only achieve locus-specific demethylation. An inducible and efficient system that drives global DNA demethylation with limited side effects has not yet been developed.

Here, to study DNAme dynamics and its impact on cellular physiology, we generated cellular models for tunable DNAme in which the DNMT1 enzyme can be inducibly degraded in a rapid and efficient manner through an auxin-inducible degron (AID) system. This tool relies on a degron, a short amino acid sequence that, when fused to a protein of interest, is able to trigger its rapid degradation by the proteasome in the presence of auxin (indol-3-acetic acid [IAA]) and the plant-derived E3 ubiquitin ligase *Os*TIR1 (*Oryza sativa* TIR1) (Natsume et al., 2016; Nishimura et al., 2009). Contrarily to other commonly used depletion approaches, the AID allows rapid (within minutes) and complete protein degradation suitable to investigate the immediate consequences of protein loss; besides, its reversibility allows to apprehend the immediate biological impact relative to the presence or absence of a protein on cellular processes (Hoffmann and Fachinetti, 2018). Leveraging the advantages of the AID system, we were able to analyze the dynamics and consequences on chromatin organization and cell fitness of passive DNA demethylation through cell divisions without the toxicity caused by demethylating drugs. To further study the interdependence between DNA methyltransferase activities, we also engineered the DNMT1 degron system in a *DNMT3B*$^{-/-}$ genetic background. Here, we evaluate time-dependent changes in methylation patterns at a genome-wide level upon DNMT1 depletion and the effect on cell proliferation and chromatin organization. We also show that DNMT1 and DNMT3B can cooperate to establish and maintain CpG methylation and chromatin domain interactions in a somatic context. The advantages of this system—rapid degradation of DNMT1 leading to massive DNA demethylation, reversibility, and low impact on cell cycle progression—make these cell lines suitable for accurate DNAme studies.

Results

Generation of an inducible DNMT1 degradation system

To study DNAme dynamics, we generated a pseudo-diploid colorectal carcinoma epithelial cell line (DLD-1) and a non-transformed, diploid retinal pigment epithelial cell line (RPE-1) in which the endogenous DNMT1 protein can be rapidly degraded through the AID system (Fig. 1 A) (Holland et al., 2012; Nishimura et al., 2009).

To engineer a miniAID (A) module fused with the fluorescent protein mNeonGreen (N) at the endogenous *DNMT1* locus, we took advantage of CRISPR-Cas9 genome editing (Fig. S1 A). Single-cell clones were isolated and the edited locus was verified by PCR (Fig. S1 B) and sequencing. The selected homozygous clone (herein after named ^{NA}*DNMT1*) has a normal doubling time (1 cell generation/day) (Fig. S1 C) and proper levels of Myc-tagged OsTIR1 expression (Fig. S1 D), ensuring the function of the AID degradation system. Cell imaging analysis and immunoblot showed efficient genetic tagging and rapid degradation of the unique endogenous DNMT1 isoform in both DLD-1 and RPE-1 clones (Fig. 1, B–G; and Fig. S1, E and F). Notably, the endogenous tag on DNMT1 did not cause alteration of its expression level compared with that in wildtype (WT) DLD-1 cells, while having only a minimal effect in RPE-1 cells (Fig. S1 E).

Upon IAA-induced DNMT1 degradation in the ^{NA}*DNMT1* DLD-1 cell line for 4 days, we observed an upregulation of DNMT3B and no changes in overall DNMT3A levels (Fig. 1 D). To counteract this phenomenon and properly model the dynamics of DNA demethylation, we knocked out (KO) *DNMT3B* in the ^{NA}*DNMT1* DLD-1 background (^{NA}*DNMT1/DNMT3B*$^{-/-}$). Correct genetic DNMT3B deletion and DNMT1 degradation were confirmed by immunoblot analysis (Fig. 1 D).

A key feature and advantage of the AID system is its reversibility: after the washout (W/O) of IAA, we could indeed observe partial reaccumulation of DNMT1 within 4 days, although this was more variable in the *DNMT3B*$^{-/-}$ cells (Fig. 1 E).

DNMT1 and DNMT3B cooperate to control DNAme dynamics at different genomic loci

As DNMT1 is the major enzyme involved in DNAme maintenance, its IAA-dependent degradation is expected to result in a progressive loss of DNAme over cycles of DNA replication.

To evaluate the degree of global DNA demethylation upon DNMT1 degradation across cell generations, we performed measurement assays to analyze the 5mC levels at different time points after IAA addition (Fig. 2 A). Global DNAme levels quantified by liquid chromatography mass spectrometry (LC-MS) decreased in ^{NA}*DNMT1* and ^{NA}*DNMT1/DNMT3B*$^{-/-}$ cell lines upon IAA administration over time and could be recovered after IAA W/O (4 days), but only in the *DNMT3B* WT background (Fig. S2 A). Of note, the protein tag did not affect DNMT1 methyltransferase activity since both DLD-1 and RPE-1 ^{NA}*DNMT1* cell lines have DNAme levels comparable with their WT counterparts (Fig. S2, A and B). We also confirmed a decrease in DNAme levels using immunofluorescence against 5mC (Fig. S2, C and D).

We scored the degree of DNMT1 degradation-induced demethylation at selected genomic loci by combined bisulfite restriction analysis (COBRA) (Xiong and Laird, 1997) (Fig. 2 B) and methylated DNA immunoprecipitation (MeDIP) analyses (Weber et al., 2005) (Fig. S2 E). With these assays, we observed locus-specific methylation reduction at 48 and 96 h after IAA treatment, with some regions being more susceptible than others. COBRA analysis showed significant demethylation at Alu and Satellite II (chromosome 1; GenBank accession number X72623) repetitive sequences and at the tudor domain containing 6 (*TDRD6*) promoter, a germline gene carrying a high DNAme load in differentiated cells (Velasco et al., 2018). Four days after IAA removal (W/O), these loci partially regained their methylation, but mostly in the *DNMT3B* WT background (Fig. 2, B and C). Analogous results were obtained by MeDIP analysis of the farnesoid X (*FXR*) and the collagen alpha2 (*COL1A2*) transcription start sites (TSS), which bear different degrees of CpG island methylation in DLD-1 cells (Fig. S2 E). In this case, DNAme was fully recovered after IAA W/O even in ^{NA}*DNMT1/DNMT3B*$^{-/-}$ cells, possibly because of partial IAA-induced DNAme reduction of these loci.

To broaden our investigation on DNAme loss, we performed a genome-wide analysis through an Infinium Methylation EPIC array. This approach allowed us to investigate DNAme quantitatively across over 850,000 CpG sites. We compared DNMT1 depletion at 2 and 4 days in WT and *DNMT3B*$^{-/-}$ genetic background compared with a non-treated control and DAC-treated DLD-1 cells. DAC is a widely used demethylating agent also known to lead to DNA damage and cytotoxicity (Palii et al., 2008). Principal component analysis (PCA) showed different distribution among conditions highlighting altered global DNAme pattern of *DNMT3B*$^{-/-}$ cells compared with WT, with the major changes observed in the ^{NA}*DNMT1/DNMT3B*$^{-/-}$ cells after 4 days of DNMT1 depletion (Fig. S2 F). DAC-treated cells for 4 days were similar to ^{NA}*DNMT1* cells after 2 and 4 days of IAA-mediated DNMT1 depletion (Fig. S2 F). Probes' methylation values (β-value) showed the expected bimodal distribution of DNAme and its gradual loss with time upon IAA-mediated DNMT1 degradation at a higher level compared with DAC treatment for 4 days (Fig. 2 D).

To investigate the role and interdependence of DNMT1 and DNM3B in regulating DNAme, we identified the differentially methylated probes (DMPs) comparing the different experimental conditions in pairs (adjusted $P_{val} < 0.05$ and $\Delta\beta > 0.3$, Table S2). By comparing the analyzed DMPs to the probes' distribution on the EPIC array, we observed that DNMT1 depletion caused DNAme loss mostly in gene bodies, while DNAme loss at intergenic regions was mostly susceptible to the absence of DNMT3B (Fig. 2 E and Fig. S2 G). Upon 2 and 4 days of DNMT1 depletion via IAA addition, 106,647 ("early") and 178,529 probes, respectively, show at least 30% methylation loss with respect to the untreated control (Fig. 2 F and Fig. S2 H). Of these 178,529 probes, 79,617 lose methylation only after 4 days of IAA treatment ("late"). This additional DNAme loss likely corresponds to the time required to achieve passive demethylation via the DNA replication cycle. The total demethylation achieved using this system was approximately four times higher than that obtained with DAC treatment (43,790 hypomethylated probes with $\Delta\beta > 0.3$ compared with untreated control), highlighting the advantage of our genetic system to study DNAme dynamics over

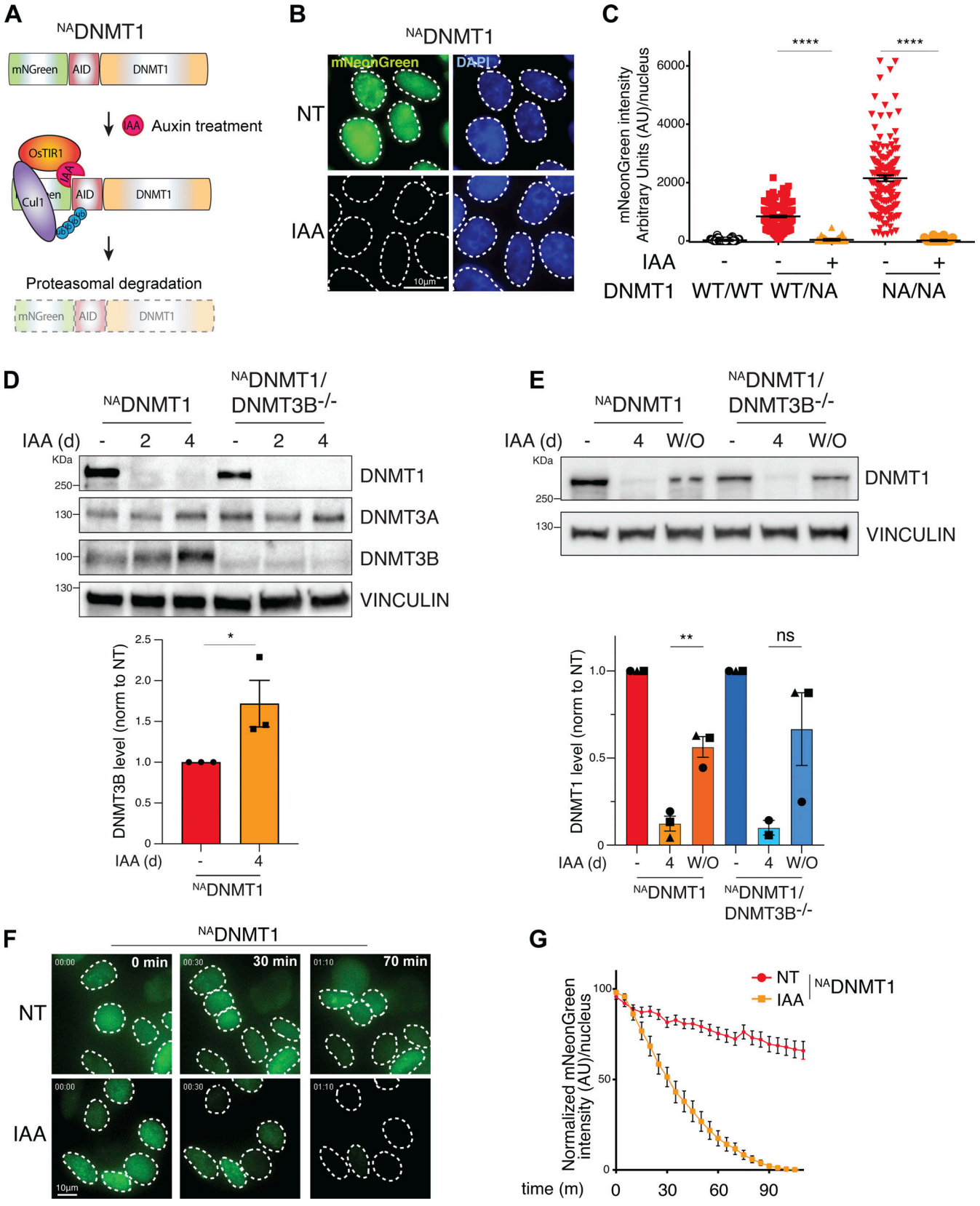

Figure 1. **Inducible, rapid, and complete DNMT1 degradation. (A)** Schematics of the endogenous *DNMT1* gene tagging strategy to achieve protein degradation. OsTIR1: *Oryza Sativa* TIR1; Cul1: Ubiquitin ligase; Ub: ubiquitin. **(B)** Representative immunofluorescence analysis of ^{NA}*DNMT1* DLD-1 cells showing mNeonGreen-tagged DNMT1 signal (NT) and its degradation upon IAA treatment (24 h). Scale bar: 10 µm. **(C)** Quantification of nuclear mNeonGreen signal (DNMT1) in the indicated DLD-1 cell clones in untreated and IAA-treated conditions (24 h). +/+: WT; +/NA: heterozygous *DNMT1*-tagged clone; NA/NA:

homozygous clone. Error bar represents the SEM; each dot represents one analyzed nucleus (n > 100 per condition). Unpaired t test: ****P < 0.0001. **(D)** Immunoblot analysis of DNMT protein levels in the indicated DLD-1 cell lines treated with IAA for 2 and 4 days (d) compared with untreated control. VINCULIN served as loading control. DNMT3B quantification normalized to VINCULIN and untreated control is also shown. N = 3. Unpaired t test: *P = 0.0265. **(E)** Immunoblot analysis and relative quantification showing DNMT1 reaccumulation after IAA W/O (4 days) in the indicated DLD-1 cell lines. VINCULIN served as loading control. DNMT1 levels were normalized to VINCULIN and untreated control. N = 3. Unpaired t test: **P = 0.0039. **(F and G)** Representative live-cell imaging (F) and relative quantification analysis (G) showing rapid DNMT1 depletion at the indicated times from IAA treatment in DLD-1 ^{NA}*DNMT1* cells. Each dot represents the mean value of analyzed cells per time point (n = 16 per condition). Error bar represents the SEM. Scale bar: 10 µm. m, min. Source data are available for this figure: SourceData F1.

common demethylating agents. Importantly, most of these DMPs did not lose DNAme in the *DNMT3B* null context, but the degree of demethylation at these sites is stronger in the KO background upon 4 days of DNMT1 depletion, suggesting a cooperative effect of DNMT1 and DNMT3B in maintaining DNAme (Fig. 2 F).

To examine the role of DNMT3B in maintaining DNAme, we compared the untreated ^{NA}*DNMT1* with ^{NA}*DNMT1/3B*$^{-/-}$ cell lines (Fig. 2 G). We identified a total of 46,739 DMPs (adj. Pval < 0.05), and only 30% of them (13,958) lost methylation in the *DNMT3B* KO versus WT. Indeed, 70% of the identified DMPs (32,781) displayed an increased DNAme status compared with control (genomic snapshots of representative loci are shown in Fig. S3 A), which is lost after 4 days of DNMT1 depletion (Fig. 2 G). This DNMT1-dependent DNAme suggests an uncontrolled DNMT1 activity in the absence of DNMT3B, at least in the isolated KO clone, which is not caused by DNMT1 upregulation in ^{NA}*DNMT1/3B*$^{-/-}$ cells (Fig. 1 D). To investigate a possible activity of DNMT3A in the locus-specific hypermethylation of ^{NA}*DNMT1/3B*$^{-/-}$ cells, we knocked down *DNMT3A* by CRISPR-Cas9 (Fig. S3 B). *DNMT3A* silencing in ^{NA}*DNMT1/3B*$^{-/-}$ cells did not cause DNMT1 upregulation (Fig. S3 B) and had only a minor effect on the global DNAme level (Fig. S3 C), suggesting a limited activity of DNMT3A in the absence of DNMT3B. Moreover, IAA-induced DNMT1 depletion in ^{NA}*DNMT1/3B*$^{-/-}$ *DNMT3A* knockdown and ^{NA}*DNMT1/3B*$^{-/-}$ cells had a similar impact on DNAme loss (Fig. S3 C). These observations were confirmed by assessing DNAme by COBRA at specific hypermethylated loci identified in ^{NA}*DNMT1/3B*$^{-/-}$ cells. DNAme at these regions is not affected by DNMT3B or DNMT3A loss, while DNMT1-induced degradation caused dramatic 5mC reduction (Fig. S3 D). Taken together, we exclude a role for DNMT3A in hypermethylating specific regions in ^{NA}*DNMT1/3B*$^{-/-}$ cells, but rather we show that this is DNMT1 dependent.

Next, we assessed the contribution of DNMT1 to DNAme in the absence of DNMT3B (Fig. 2 H). DNMT1 depletion in the *DNMT3B*$^{-/-}$ genetic background had the greatest effect on demethylation, with 455,309 total DMPs (P_{val}< 0.05 and Δβ > 0.3). These probes showed higher methylation levels when DNMT3B is expressed, indicating that DNMT1 and DNMT3B act cooperatively. Even at these DMPs, DAC was less efficient in inducing CpG demethylation. To investigate the DNAme activity of DNMT3B in a DNMT1 null context, we compared 4-days IAA-treated ^{NA}*DNMT1* versus 4-days IAA-treated ^{NA}*DNMT1/3B*$^{-/-}$ cells, and we identified 5,213 DMPs (P_{val}< 0.05 and absolute Δβ = 0.3) (Fig. 2 I). Also in this case, we observed a cooperative activity of DNMT1 and DNMT3B since 4-days IAA-treated ^{NA}*DNMT1/3B*$^{-/-}$ cells showed higher level of DNAme loss of most of the probes (4,523) compared with untreated ^{NA}*DNMT1/3B*$^{-/-}$ cells (Fig. 2 I). Similarly to what we observed in the ^{NA}*DNMT1/3B*$^{-/-}$ cells (Fig. 2 G), among the aforementioned 5,213 DMPs, we identified 690 DMPs whose methylation level was higher in the absence of DNMT3B. This could be due to residual DNMT1 activity, compensatory mechanisms, and/or to a lesser sensitivity to demethylation since their methylation load is high in untreated ^{NA}*DNMT1/3B*$^{-/-}$ cells (Fig. 2 I).

To investigate if the DMPs regulated by DNMT1 and DNMT3B are located in specific epigenetic contexts, we took advantage of the ChromHMM tracks that categorize the chromatin states of the human genome into 15 categories (Ernst and Kellis, 2017). By comparing the analyzed DMPs to the probes' distribution on the EPIC array, DNMT1 depletion preferentially induced progressive hypomethylation at facultative heterochromatin (Polycomb-repressed sites), transcription transition and elongation sites, and weakly transcribed sequences and enhancer elements, while DNAme at active promoters was unaffected (Fig. S3 E). DNAme loss at Polycomb-repressed regions was also observed in *DNMT3B*$^{-/-}$, with additional changes occurring at constitutive heterochromatin and insulators. In contrast, DNMT3B loss had no impact on transcriptionally active loci and strong enhancers and, as with DNMT1, DNAme at active promoters was unaffected (Fig. S3 F). In addition, using the Repeat Masker tool (https://www.repeatmasker.org) (Jurka, 2000), we assessed how DNMT1 and DNMT3B affect DNAme levels at repetitive genome elements. DNMT1 had a major impact on LINE (long interspersed nuclear elements) and SINE (short interspersed nuclear elements) and DNA repeats (Fig. S3 G). While DNMT3B loss had the same effect on LINE elements, it had no impact on SINEs and DNA repeats; unlike DNMT1, we observed DNMT3B-dependent demethylation of LTRs (long terminal repeats) (Fig. S3 H). Together, this suggests some degree of targeting of the enzymes to different types of chromatin, with DNMT3B acting more specifically on heterochromatin (according to ChromHMM and LINE-rich regions), while DNMT1 acts more broadly in both euchromatin and heterochromatin (as evidenced by ChromHMM and its effect on both LINE- and SINE-rich regions).

Conditional DNMT1 depletion partially impairs cell proliferation, while codepletion with DNMT3B leads to cell lethality

To assess the effect of gradual DNA demethylation on cell proliferation and survival without the secondary effects of chemical demethylating agents (Jüttermann et al., 1994), we performed cell cycle analysis in p53-mutated (Liu and Bodmer, 2006) DLD-1 ^{NA}*DNMT1* and ^{NA}*DNMT1/3B*$^{-/-}$ cells with up to 10 days of IAA-mediated DNMT1 degradation (Fig. 3 A and Fig. S4 A). After

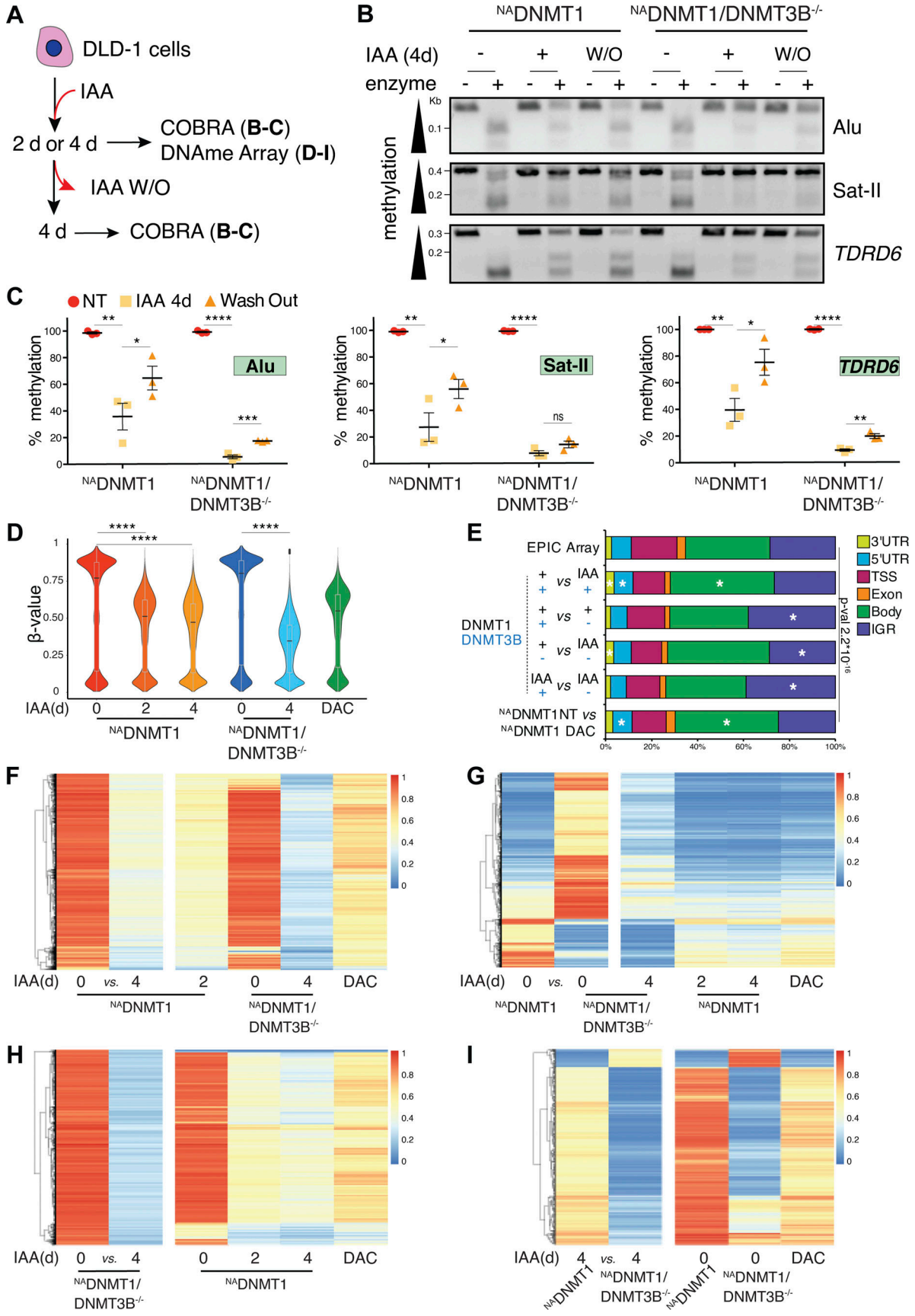

Figure 2. **Induced DNMT1 degradation leads to progressive DNA demethylation. (A)** Schematics of the experiments shown in panels B–I. **(B)** Representative agarose gel of COBRA at selected loci in the indicated cell lines and treatment conditions. BstUI and BstBI enzymes were used for *TDRD6*, Alu and

Satellite II, respectively. **(C)** Quantification of methylated DNA (as percentage of total DNA) at the indicated regions by COBRA assay normalized to relative untreated control. Each dot represents one biological replicate (N = 3); error bars represent the SEM. Unpaired t test: Alu: *P = 0.049, **P = 0.017, ***P = 0.006, ****P < 0.0001; Satellite II: *P = 0.0456, **P = 0.013, ****P < 0.0001, n.s. = not significative; *TDRD6*: *P = 0.0255, **P = 0.001 and 0.003; ****P < 0.0001. **(D)** Combined violin-box plot showing the distribution of methylation β-values of probes identified by the EPIC array in the indicated cell line and conditions. Dark line indicates the medians; boxes indicate Q1 and Q3; whiskers extend to include 99% of the data. Wilcoxon sum rank test: ****P < $2.2*10^{-16}$. DAC: 4 days (d), 2.5 μM. **(E)** Genome annotation analysis of the DMPs identified in the indicated pair comparisons. The distribution of the EPIC array probes is shown as a reference. IGR: intergenic regions. A chi-square test was used to calculate P values and define significant changes in the distribution of DMPs of the indicated categories relative to EPIC array composition. Stars (*) indicate the genomic loci with major changes (i.e., contributing the most to the P value based on the standardized residuals, stdres > 2, calculated by R software). **(F–I)** Heatmap showing methylation intensity of DMPs (P < 0.05, Δβ-value ≥ 30%) among the indicated cell lines and conditions. The first two columns represent the DMPs identified in the indicated pairwise comparison. The methylation status of the same DMPs in the other cell lines and treatment conditions is also shown. Due to the limited capacity of graphical visualization of high number of DMPs, in F are shown 40,697 DMPs (Δβ-value ≥ 40%) out of 106,647 (Δβ-value ≥ 30%) as indicated in the text; in G are shown 18,874 DMPs (Δβ-value ≥ 40%) out of 46,739 (Δβ-value ≥ 30%) as indicated in the text; similarly, in H are shown 12,381 DMPs (Δβ-value ≥ 60%) out of 455,309 as stated in the text (Δβ-value ≥ 30%). DAC: 4 days, 2.5 μM. Number of identified DMPs between conditions are reported in Table S2. Source data are available for this figure: SourceData F2.

8–10 days of IAA treatment, we observed an increased percentage of cells in G1 and a reduced S phase (Fig. 3 B), indicating that DNMT1 depletion over time impaired the cycling rate. These defects in cell cycle progression were further enhanced in the absence of DNMT3B: here, cells started to accumulate in G1 after just 4 days of depletion, and the impact on the percentage of cells in S phase was more pronounced. DNMT1/3B co-depleted cells, but not single DNMT1-depleted cells, showed an increased percentage of sub-G1 positive cells suggesting cell death (Fig. 3 A and Fig. S4 A). Following DNMT1 depletion, the arrest in G1 occurred faster in the p53-proficient diploid RPE-1 cells compared to p53-mutated (S241F) DLD-1 cells (Fig. S4 B). Accordingly, we observed an accumulation of p53, p21, and p16 proteins following DNMT1 degradation (Fig. S4 C), proving the activation of the cell cycle checkpoint in response to the DNAme loss.

To assess the consequences of DNMT1 and/or DNMT3B depletion on cell proliferation, we performed a dye-free, live-cell imaging analysis for 6 days on IAA-treated or untreated cells. While DNMT1 and DNMT3B single-depleted cells showed lower proliferation rates than WT cells, simultaneous depletion of DNMT1 and DNMT3B had a major effect on cell fitness (Fig. 3 C). The long-term effects of DNMT1 depletion in WT and *DNMT3B*$^{-/-}$ cells were then assessed by colony formation assay after 12 days of IAA treatment. While DNMT1 depletion in ^{NA}*DNMT1* cells has a mild but detectable effect on cell survival (Fig. 3, D and E), 6 days of IAA pretreatment before seeding drastically impaired colony formation and survival. In agreement with the observed faster G1 arrest, inhibition of cell proliferation was stronger in the ^{NA}*DNMT1* RPE-1 cell line following DNMT1 depletion (Fig. S4 D). This is in agreement with the p53-dependent apoptosis and p21 upregulation observed in *DNMT1* KO mouse embryonic fibroblasts (Jackson-Grusby et al., 2001). In line with the live-cell imaging results, DNMT1 and DNMT3B codepletion halted colony formation (Fig. 3, D and E). In addition, the reduced colony formation potential observed after single DNMT1 depletion was rescued by IAA removal, but not in the *DNMT3B* KO background (Fig. 3, D and E). However, high numbers of mitotic errors are unlikely to be the cause of the reduced proliferation potential observed in ^{NA}*DNMT1/3B*$^{-/-}$ IAA-treated cells, as copy number variation (CNV) analysis by single-cell sequencing revealed low levels of aneuploidy compared with untreated ^{NA}*DNMT1/3B*$^{-/-}$ cells (20% in IAA versus 12.2% in untreated; Fig. S4 E). Treatment with the hypomethylating agent DAC had a stronger effect on cell proliferation (Fig. 3 D) despite causing a smaller reduction of DNAme with respect to IAA-induced DNMT1 depletion (Fig. S4 F and Fig. 2 F), highlighting a DNAme-independent cytotoxic effect. Recently a new, more tolerable and less toxic DNMT1 inhibitor was developed for chemotherapeutic purposes (GSK3685032 [Pappalardi et al., 2021]). The treatment of ^{NA}*DNMT1* DLD-1 cells with different doses of GSK3685032 led to a milder demethylation compared with the one obtained by IAA-induced DNMT1 degradation for the same amount of time (Fig. S4 F). At the highest and most efficient concentration tested, GSK3685032 had, however, a significant effect on cell proliferation than IAA-induced DNMT1 depletion (Fig. S4 G), suggesting some level of DNAme-independent toxicity. Overall, this suggests that prolonged GSK3685032 and DAC treatments affect cell growth while having less demethylating efficiency with respect to induced DNMT1 depletion for the same treatment duration. Taken together, these data demonstrate that DNAme level is necessary to maintain proper cell proliferation.

DNA methyltransferase loss disrupts subnuclear compartmentalization of inactive chromatin states

DNAme is deposited at CpGs of most inactive regulatory elements that are normally confined to heterochromatin and inactive regions marked by H3K9me3 or H3K27me3, respectively (Rose and Klose, 2014). Moreover, it has been proposed that DNAme can influence H3K9me3 deposition (Lehnertz et al., 2003). To assess the interdependence between DNAme and heterochromatin, we implemented a hybrid cytometry-microscopy (Imagestream) coupled to ad-hoc image analysis by which we tested the subnuclear localization of such histone posttranslational modifications (PTMs) upon induced demethylation (Fig. 4 A and Fig. S5 A). H3K9me3 was typically expected to correlate with DNA density and was shown to be mainly positioned at pericentromeres and the nuclear periphery in fully differentiated cells (Padeken and Heun, 2014; Sánchez et al., 2019). Upon DNMT1 depletion, H3K9me3 and H3K27me3 marked regions delocalize from the nuclear periphery to the nucleoplasm (Fig. 4, A–C). This effect was further enhanced by simultaneous DNMT1 and DNMT3B depletion. DNMT1 re-expression rescued the localization of H3K9me3 and H3K27me3 positive loci to the nuclear periphery, but only partially in ^{NA}*DNMT1/3B*$^{-/-}$ cells (Fig. 4, A–C).

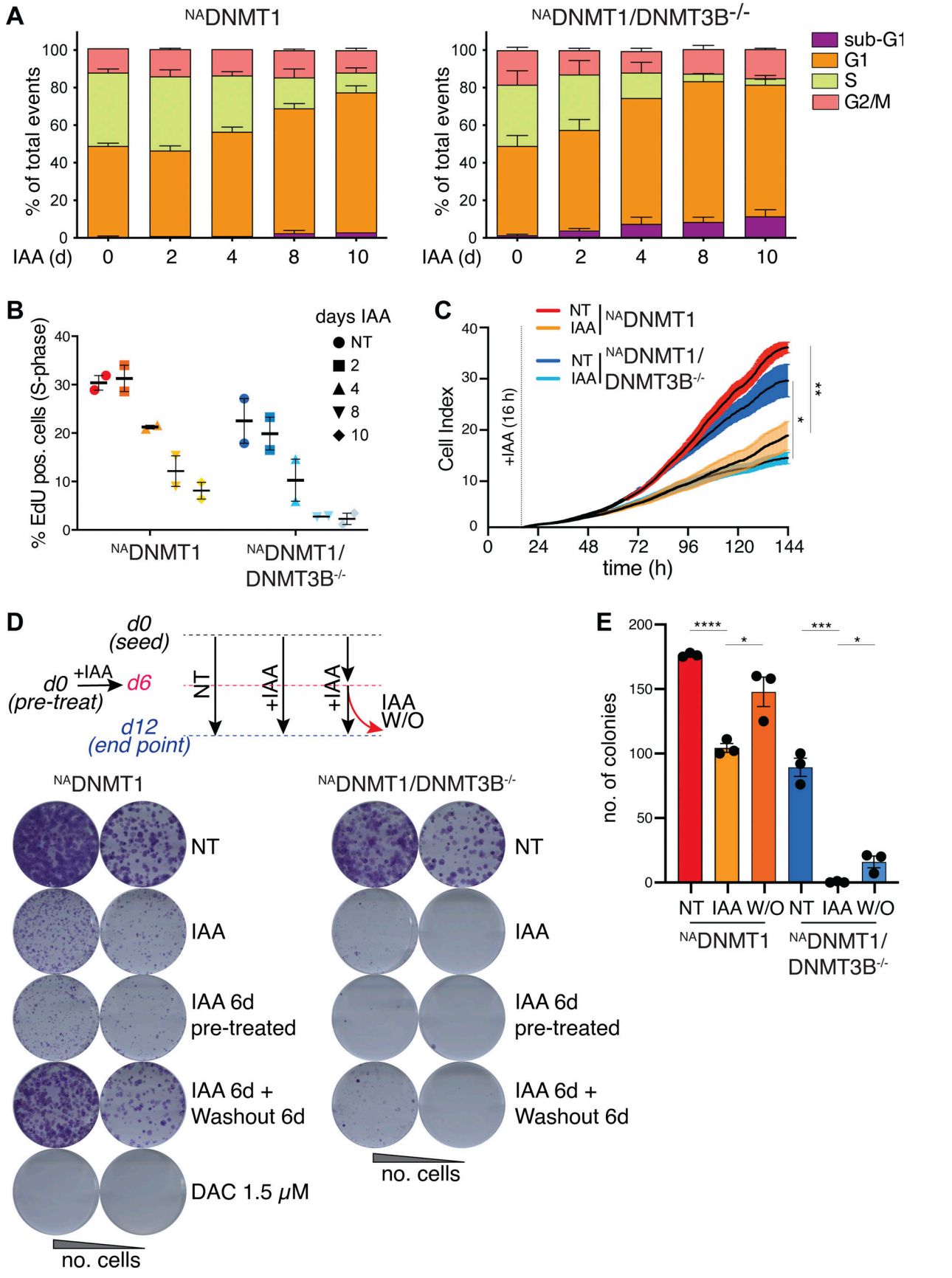

Figure 3. **DNMTs degradation impairs cell proliferation. (A)** Cell cycle profiling by EdU/DAPI incorporation upon induced DNMT1 degradation at the indicated days from IAA treatment in DLD-1 *NADNMT1* (left) and *NADNMT1/DNMT3B*$^{-/-}$ cells. *N* = 2, Error bars represent SEM. **(B)** Quantification of S phase (%

over the total) from A in the indicated cell lines and treatment conditions. Dots represent biological replicates (N = 2); bars represent the mean with SEM. **(C)** Real-time cell index measurement of the indicated DLD-1 cell lines upon IAA treatment. Measurements were normalized to the 16 h time point, time of IAA addition after seeding. Curves represent the mean cell index value from triplicates ± SD (N = 3). Unpaired t test: **P = 0.0044; *P = 0.0268. **(D and E)** Representative images of colony formation assay and relative schematics and quantifications performed in the indicated DLD-1 cell lines and treatment conditions. Number of colonies obtained in selected conditions are plotted in E. N = 3. Error bars represent SEM. Unpaired t test: ****P < 0.0001; ***P = 0.002; *P = 0.025, 0.021. d, day.

These results prompted us to investigate the genome organization following DNAme changes. Chromosome conformation capture (Hi-C) maps revealed that the genome segregates into two main chromatin compartments (A and B) (Imakaev et al., 2012; Lieberman-Aiden et al., 2009), which broadly correlate with active and inactive chromatin, respectively. Higher resolution Hi-C allowed a finer classification into active and inactive subcompartments (A1-A2 and B0-B4, respectively) (Rao et al., 2014; Spracklin et al., 2023). We therefore performed in situ Hi-C on untreated and treated (4 d and 10 d IAA) ^{NA}*DNMT1* and ^{NA}*DNMT1/3B*$^{-/-}$ DLD-1 cells, as well as in ^{NA}*DNMT1* after IAA W/O. First, we compared P(s) curves, which reflect the size and density of extruded loops, and observed no significant differences between conditions, suggesting that loss of DNAme does not alter the levels of cohesin-mediated loop extrusion (Fig. S5 B). These data also suggest that the cell cycle arrest observed in the induced degron system does not dramatically alter contact frequency. To assess the effect of DNMT1 depletion on subnuclear compartmentalization of the genome, we next analyzed long-range contact frequencies using a recently published method (Spracklin et al., 2023). While conventional compartmentalization analysis quantifies preferential interactions by imposing a binary A versus B classification, this approach partitions genomic loci–based on more complex patterns of long-range interactions into groups termed subcompartments or interaction profile groups (IPGs). As in Spracklin et al. (2023), our analysis disregards purely position-dependent effects on long-range interactions by consolidating clusters of loci that share a common epigenetic signature but differ in their genomic distance from the centromere (Fig. S5 C). Using this approach, we identified two transcriptionally active IPGs that we labeled DLD-A1 and DLD-A2, with the former having the strongest transcriptional activity and highest GC (guanine-cytosine) content, following a similar naming trend as in other cell types. With a limited set of functional annotations, we decided not to assign a special label to clusters V and VI showing intermediate transcriptional activity. We further identified two broadly transcriptionally inactive (or heterochromatic) IPGs: DLD1-B4 and DLD1-B2/3. We assigned the label DLD1-B4 based on its epigenetic setting and positional similarity of its loci to B4 subcompartment regions in GM12878 cells (Rao et al., 2014), as well as its epigenetic similarity to the B4 IPG detected in HCT116 cells (Spracklin et al., 2023). Specifically, we observed that DLD1-B4 is the only IPG enriched for the constitutive heterochromatin mark H3K9me3 and, as in the GM12878 cell line, it is primarily located pericentrically and on chromosome 19 (Fig. S5 C).

Recently, it was observed that the B4 IPG identified in HCT116 and its associated H3K9me3/HP1 chromatin state was disrupted under 5aza-mediated chemical inhibition of DNA methyltransferases and joint long-term perturbation of DNMT1 and DNMT3B using genetic KO cells (Spracklin et al., 2023). Consistent with these results, we found that DLD1-B4 compartmentalization was also disrupted under inducible DNMT1 degradation. This occurred in a time-dependent manner, reaching a roughly twofold reduction in the average observed-over-expected contact frequency between DLD1-B4 loci in both genetic backgrounds after 10 days of IAA treatment (Fig. 4, D–F). To validate this effect at the epigenome level, we performed chromatin immunoprecipitation sequencing (ChIP-seq) for H3K9me3 in untreated ^{NA}*DNMT1* and in untreated and 10 days treated ^{NA}*DNMT1/3B*$^{-/-}$. We found that the loss of compartmentalization after treatment is accompanied by a dramatic global reduction of H3K9me3 levels (Fig. 4, F and G, Fig. S2 G, Fig. S3 A, and Fig. S5 E) with little effect on H3K27me3 levels (Fig. S5, D and E). We also observed that untreated ^{NA}*DNMT1/3B*$^{-/-}$ cells displayed weaker DLD1-B4 self-affinity and reduced H3K9me3 levels compared with untreated ^{NA}*DNMT1* (Fig. 4, D and G; and Fig. S5 F), suggesting that DLD1-B4 is mildly impacted by DNMT3B depletion; however, we cannot rule out if this could be due to minor differences in baseline DNMT1 levels in the two backgrounds (Fig. 1 D). Importantly, we observed that the impact of DNMT1 depletion on compartmentalization was reversible: after 4 days of IAA W/O in ^{NA}*DNMT1* cells previously treated for 4 days with IAA, DLD1-B4 self-interaction in cis and in trans recovered to ∼80% (Fig. 4 E and Fig. S5 F).

The second inactive IPG detected in untreated ^{NA}*DNMT1*, which we label DLD1-B2/3, covers ∼30% of the mappable autosomal genome in these cells and has an incompletely characterized chromatin state, though it exhibits a dispersed enrichment for H3K27me3 (according to GSE85688, (Rokavec et al., 2017), suggesting that this state is at least partially heterochromatic (Fig. S5 C). The majority of loci of this IPG were assigned to the transcriptionally inactive subcompartment labels B2 and B3 in other cell types by SNIPER (subcompartment inference using imputed probabilistic expressions) (Xiong and Ma, 2019), a supervised learning algorithm that generalizes GM12878 subcompartment labels to other cell types (Fig. S5 G). Interestingly, we found that self-interaction and compartmentalization of DLD1-B2/3 were significantly disrupted in the ^{NA}*DNMT1/3B*$^{-/-}$ genetic background, irrespective of IAA treatment duration (Fig. 4 D and Fig. S5 H). These results imply that a different DNA methyltransferase, DNMT3B, is required to maintain a different inactive IPG, DLD1-B2/3, suggesting a separation of function for DNMT3B and DNMT1 in genome organization. Interestingly, the median hypermethylation effect (attributed to DNMT1 uncontrolled activity in *DNMT3B* KO cells) is slightly stronger on CpGs in the DLD1-B2/3 subcompartment (Fig. S5 I). This suggests that the uncontrolled methylation activity of DNMT1 in the absence

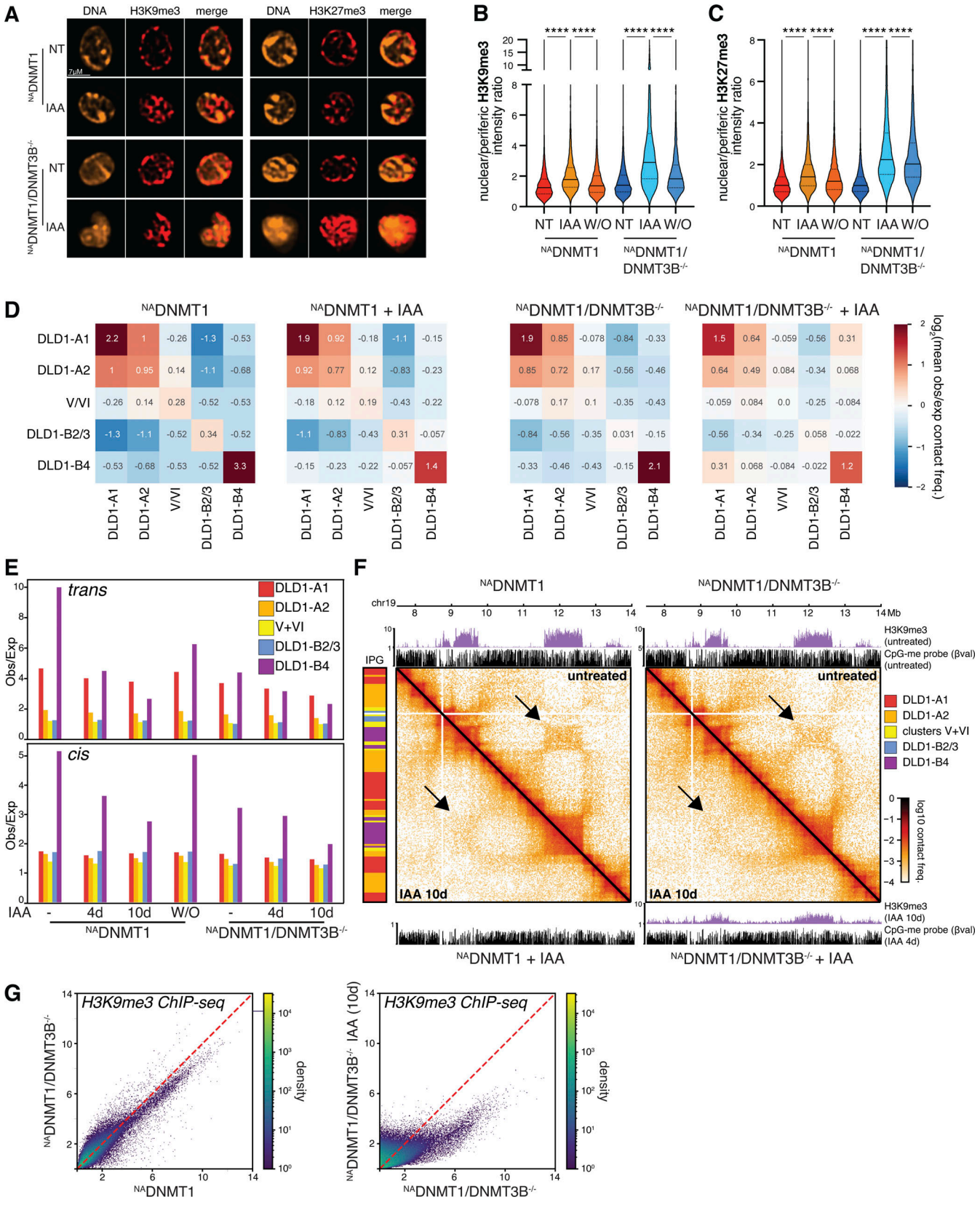

Figure 4. **DNMTs sustain subnuclear compartmentalization of inactive chromatin. (A)** Representative immunofluorescence images of hybrid microscopy-cytometry analysis of H3K9me3 and H3K27me3 on the indicated DLD-1 cell lines and conditions (IAA: 10 days). Scale bar: 7 µm. **(B and C)** Ratio of the nuclear H3K9me3 (B) and H3K27me3 (C) signal intensities over the signal measured at the nuclear periphery by hybrid microscopy-FACS analysis in the indicated cell lines and conditions. IAA: 10 days. W/O experiments were analyzed 4 days after IAA removal (IAA: 6 days). Each point represents the ratio value

for one single nucleus. *n* = 1,375–15,005 cells per condition. Wilcoxon Signed Rank Test: ****P < 0.0001. **(D)** Heatmaps of pairwise aggregate observed/expected contact frequency between IPGs, derived from 50-kb resolution contact maps for untreated and 10-days IAA-treated *^{NA}DNMT1* cells and untreated and 10 days IAA-treated *^{NA}DNMT1/DNMT3B$^{-/-}$* cells, respectively. **(E)** Time courses of observed/expected contact frequency in trans (top) and in cis (bottom) within the same five defined IPGs in the indicated cell lines and conditions. The W/O experiment was analyzed 4 days (d) after IAA withdrawal (IAA: 4 days). **(F)** Example of DLD1-B4 disruption on a region of chromosome 19 in *^{NA}DNMT1* (left) and *^{NA}DNMT1/DNMT3B$^{-/-}$* (right) after 10 days of IAA treatment. Top to bottom: tracks of H3K9me3 (fold change over input) and CpG methylation (SWAN-normalized β-values from EPIC array analyses) signal in untreated cells, Hi-C from untreated (top right) and treated cells (bottom left), tracks of H3K9me3 and CpG methylation from treated cells. Left: Colored track of IPG classification derived from untreated *^{NA}DNMT1* cells. Arrows point to a zone of distal DLD1-B4 interaction that is visibly depleted upon treatment. **(G)** Scatter plot showing loss of H3K9me3 ChIP-seq signal density (mean fold change over input) upon DNMT3B deletion (left) and DNMT1 depletion (10 days, right) in *^{NA}DNMT1/DNMT3B$^{-/-}$* cells. Each point represents a 10-kb genomic bin.

of DNMT3B may have a bias for heterochromatic regions with a peculiar uncharacterized chromatin state.

Discussion

Studies of DNAme and its dynamics have been challenging because current methods to specifically manipulate DNAme have low efficiency and high toxicity. Our newly generated cell models enable us to assess acute, reversible, and time-dependent effects of DNMT1 loss and DNAme reduction on cell physiology, providing valuable information without bias due to cytotoxicity and cell adaptation to constitutive long-term protein depletion. A similar strategy for DNMT1-inducible degradation has been established in HCT116 cells for structural studies on DNMT1 activation (Kikuchi et al., 2022). Using our DNMT1 degradation system, we demonstrate the essential roles of both DNMT1 and DNMT3B in achieving and maintaining defined DNAme patterns across the genome, acting both independently and in cooperation. The observed DNMTs' joint activity is in agreement with previous reports showing DNAme loss in hypomorphic *DNMT1/DNMT3B* KO HCT116 cells (Cai et al., 2017; Rhee et al., 2002). The presence of genomic loci gaining DNAme in a DNMT1-dependent manner only in *DNMT3B$^{-/-}$* cells spotlights a non-canonical or uncontrolled de novo DNMT1 methyltransferase activity at selected genomic loci, which, based on previous in vitro (Fatemi et al., 2001; Vilkaitis et al., 2005) and in vivo experiments, was proposed to be limited to transposable elements (Haggerty et al., 2021), non-CpG sites (Grandjean et al., 2007), and selected promoters (Peters et al., 2013). In this context of a compensatory role for DNMT1 in de novo methylation at selected loci, we rule out the potential involvement of DNMT3A activity. Given the reversibility of DNMT1 degradation upon IAA removal, this system proves invaluable for studying the dynamic processes of CpGs remethylation.

While our DNMT1 degradation system effectively induces a genome-wide reduction in DNAme, we show that heterochromatic regions are particularly susceptible to DNA demethylation. Our Hi-C results indicate that (i) 3D compartmentalization of the DLD1-B4 IPG is progressively and reversibly sensitive to loss of DNMT1, while (ii) that of the DLD1-B2/3 IPG is sensitive to the loss of DNMT3B. In DLD1 cells, DNMT1 loss induced isolated but reversible changes in the preferential interaction of H3K9me3 chromatin domains found in pericentromeres and on chromosome 19. This stands in contrast to DNMT1 loss in the HCT116 cell line, where H3K9me3 domains cover a much greater proportion of the genome, thus leading to a more widespread phenotype on contact maps (Spracklin et al., 2023). Conversely, we show that the preferential interaction of the chromatin state underlying the B2/3 IPG, which appears to be absent in HCT116 but is the most abundant silent IPG in DLD1 cells, depends on a different methyltransferase, DNMT3B. Collectively, our findings unveiled the complementary roles played by distinct DNMTs in preserving defined chromatin states.

The recovery of DLD1-B4 compartmentalization upon IAA withdrawal was rapid and near complete (Fig. S5 F), while DNAme recovery was partial (Fig. 2 B and Fig. S2 A). This suggests that specific CpG sites may be critical, but also raises the possibility that DNMTs regulate broad heterochromatic regions in a manner that is not directly coupled to their DNAme activity. Likewise, additional factors, such as proteins of the methyl-CpG-binding domain family, may contribute to heterochromatin maintenance. Dissecting these regulatory connections and understanding their contributions to the formation of cell-type-specific heterochromatic landscapes will be the focus of future research.

Beside the effect on heterochromatin regions, depletion of DNMT1 causes the active DLD1-A1 and DLD1-A2 IPGs to exhibit decreased self-interaction preference and increased preference for interacting with inactive IPGs. These data indicate an overall reduction in compartmental segregation when heterochromatin is lost (Fig. 4, D and E). Taken together, our results highlight the interplay between DNAme, heterochromatin, and genome organization (Gilbert et al., 2007; Matarazzo et al., 2007), and suggest that DNMTs have a significant role to play in long-range genome organization, in agreement with previous reports (Du et al., 2021; Spracklin et al., 2023).

In conclusion, our inducible system serves as a powerful tool to elucidate in greater detail the mechanisms and temporal dynamics driving DNMT-dependent heterochromatin formation and 3D genome regulation. Further questions remain to be elucidated. For example, the DNMT1-controlled IPG domains on chromosome 19 contain clusters of Zinc finger proteins. It would be interesting to investigate if these factors are transcriptionally dependent on DNMT1 and contribute to cell homeostasis. The depletion of DNMT3B alone triggers a loss of affinity of chromatin domains bearing features of facultative heterochromatin. This likely corresponds to the observed chromatin delocalization from the nuclear periphery to the inner nuclear space, as revealed by hybrid microscopy/FACS analyses. These disrupted interactions could coincide with lamin-associated domains. Similarly, our system could be leveraged to study the functional link between DNAme and histone PTMs.

Finally, in sharp contrast to previous reports using an inducible *DNMT1* KO in HCT116 colorectal cancer cells (Chen et al., 2007), we found that complete DNMT1 depletion did not lead to rapid and severe cell lethality and/or mitotic failure. Our data emphasize that the observed cellular fitness defects are not primarily attributed to the loss of DNMT1 itself, but, rather, to the progressive decrease in DNAme. The strong additive effect on cell survival in the double DNMT1/3B-depleted cells is therefore the consequence of decreased 5mC levels as DNAme is strongly reduced in the double mutant. We hypothesize that the severe cell cycle arrest and cell death observed after only 48 h of genetic deletion of selected exons of the *DNMT1* gene (Chen et al., 2007) may be due to non-specific toxic effects (e.g., from Cre recombinase expression [Loonstra et al., 2001]). Recently, long-term (6 weeks) partial downregulation of *DNMT1* was shown to promote high level of aneuploidy in RPE-1 cells (Besselink et al., 2023), in contrast to what we observed (Fig. S4 E). We propose that our DNMT1 depletion system is better suited for studying the consequences of DNAme reduction in both normal (e.g., RPE-1) and tumoral (e.g., DLD-1) contexts since DNMT1 degradation is complete and temporally controlled. Moreover, although recent efforts have been made toward the generation of less toxic demethylating agents (e.g., GSK3685032 [Pappalardi et al., 2021]), the cell lethality upon DNMT1-induced degradation is lower than that observed in cells treated with traditional demethylating drugs. In summary, we assert that the distinctive features and advantages of our cellular models—namely, reversibility, temporal control, and absence of DNAme-independent toxicity—render them indispensable tools for future investigation into fundamental biological questions concerning the role of DNAme, its establishment, and maintenance.

Materials and methods

Cell culture and treatments

Cells were cultured at 37°C in a 5% CO_2 atmosphere. DLD-1 (RRID: CVCL_0248; ATCC) and immortalized hTERT RPE-1 cells (RRID: CVCL_4388; ATCC) were maintained in DMEM-GlutaMAX and DMEM:F12 media, respectively, supplemented with 10% fetal bovine serum, 100 U/ml penicillin-streptomycin, and 0.13% sodium bicarbonate (RPE-1). IAA (I5148; Sigma-Aldrich) was used at 500 nM dissolved in water. DAC (A3656; Sigma-Aldrich) was used at 2.5 µM for 96 h. GSK-3685032 (HY-139664; MedChemExpress) was used at the indicated time and concentrations. All cell lines were tested negative for mycoplasma contamination. IAA W/O was performed by five gentle washes in PBS. Cells were then analyzed at the indicated time points.

Plasmids and cell line generation

The repair template containing mNeonGreen-miniAID sequence flanked by left and right homology arms (±500 bp from ATG) of *DNMT1* genomic sequence was cloned into pCR-BluntII-TOPO plasmid with the Zero Blunt TOPO PCR Cloning Kit (Thermo Fisher Scientific). The *DNMT1*-targeting sgRNA (5′-GGCGGTACG CGCCGGCATCT-3′) was cloned into pX330 hSpCas9 expressing vector (#42230; Addgene) and verified by sequencing.

DLD-1 and RPE-1 cells stably expressing OsTIR1-Myc9 were nucleofected with the DNMT1 targeting pX330 plasmid in the presence of the repair template by electroporation using the Lonza Nucleofector with appropriate reagents (Nucleofector Solution V and L for DLD-1 and RPE-1, respectively) according to the manufacturer's instructions. A molar ratio of 9:1 between the donor and the pX330 plasmid was used. 5 days after transfection, mNeonGreen-positive cells were FACS-sorted and seeded for clone isolation. Clones were amplified and screened by PCR amplification of a region outside the homology arms (forward: 5′-GCCGCCATCGAGATGCACAG-3′; reverse: 5′-CCACACACT GGGTATAGAAGTGGC-3′). Positive clones were confirmed by PCR sequencing and immunoblotting.

DLD-1 *DNMT3B*$^{-/-}$ cells were generated by lentiviral transduction with a modified pSB700 vector (plasmid #64046; RRID: Addgene_64046; Addgene) expressing a sgRNA targeting the ATG of *DNMT3B* gene (sequence: 5′-GAAGACTCGATCCTCGTC AA-3′) and H2B-mCerulean chimera. Clones were isolated, amplified, and screened by PCR genotyping and immunoblot.

DNMT3A acute KD was generated by lentiviral transduction of ^{NA}DNMT1 and ^{NA}DNMT1/DNMT3B$^{-/-}$ with a pLENTI-CRISPRv2 (plasmid #83480; RRID:Addgene_83480; Addgene) expressing an sgRNA targeting *DNMT3A* (sequence: 5′-CGATGA CGAGCCAGAGTACG-3′) (kind gift of Pierre-Antoine Defossez, Université Paris Cité, Paris, France). Cells were collected for analysis 4 days after transduction.

Colony formation assay

Serial dilutions of cells were plated on 6-well plates and 500 nM IAA was added the day after seeding. After 14 days, colonies were fixed for 10 min in methanol, washed twice with PBS 1X, stained for 10 min in 1% crystal violet and 20% EtOH, and washed twice with PBS 1X. Colonies obtained from the same serial dilution across all the analyzed conditions were quantified.

Cell proliferation assays

Cell proliferation was measured on xCELLigence (Agilent) E-Plate VIEW (96 wells) in an xCELLigence eSight real-time cell analyzer. Cells were passaged and allowed to reach 70–80% confluency before being trypsinized, counted, and resuspended in standard growth media to 4 × 10^4 cells/ml. Blanks were measured on the E-Plates with 50 µl of standard growth media before adding 50 µl of the cell suspension, equivalent to 2,000 cells, in triplicate wells per condition. Measurements were performed every 15 min and pictures of each well were taken every hour for a total of 6 days. After 16 h, an additional 50 µl of media was added to all wells, either with or without IAA to a final concentration of 500 µM per well. Cell index, i.e., the electrical impedance generated from cell attachment and proliferation quantified via gold electrodes at the bottom of the cell culture plate wells was calculated with the RTCA eSight Software (Agilent) and normalized to the 16 h time point. WST-1 cell proliferation assay was performed by seeding 0.7 × 10^3 cells per well in a 96-well plate in triplicate for each day of the growth curve. Treatments were added 24 h after seeding. For daily measurements, cells were grown for 3 h in the presence of WST-1 reagent (5015944001; Sigma-Aldrich) added at 1:10 final dilution.

The absorbance was measured at λ = 450 nm with a microplate reader (Fluostar) using λ = 690 nm as the reference wavelength. The experiment was performed in triplicate for each condition.

Cell cycle analysis

EdU pulse was performed for 30 min (10 μM final) before collection and fixation in 70% ethanol. Click reaction was carried out with homemade click chemistry buffer (Tris-HCl 100 mM, pH 8.5, $CuSO_4$ 1 mM, Azide-fluor488 5 μM, ascorbic acid 100 mM) for 30 min at room temperature. Then, propidium iodide (PI) was added at 2.5 μg/ml final concentration in the presence of 250 μg/ml RNAseA (Thermo Fisher Scientific) and incubated at least 1 h before acquisition on a LSRII Flow Cytometer (BD). Data were analyzed using FlowJo software v10 (BD). Cell doublets were excluded, and the autogating tool was applied to select G1, S, G2/M populations.

Single-cell DNA sequencing

One million cells were resuspended in media, washed, and pelleted. Cells were resuspended in cell lysis buffer (100 mM Tris-HCl, pH 7.4, 154 mM NaCl, 1 mM $CaCl_2$, 500 μM $MgCl_2$, 0.2% BSA, 0.1% NP-40, 10 μg/ml Hoechst 33358, 2 μg/ml PI in ultrapure water) and incubated on ice in the dark for 15 min to complete lysis and generate nuclei. Resulting cell nuclei were gated for G1 phase (as determined by Hoechst and PI staining) and single nuclei were sorted into wells of 96-well plates on a MoFlo Astrios cell sorter (Beckman Coulter). 96-well plates containing nuclei and freezing buffer were stored at −80°C until further processing. Single-cell whole-genome sequencing libraries preparation was prepared on a Bravo Automated Liquid Handling Platform (Agilent Technologies) as described in van den Bos et al. (2019). Briefly, genomic DNA was extracted from single nuclei, fragmented by micrococcal nuclease, end-repaired, A-tailed, and subjected to Illumina PE forked adapter ligation. After AMPure XP bead clean-up, adapter-containing DNA fragments were PCR amplified using multiplexing primers to incorporate library-specific barcodes. Pooled libraries were sequenced on a NextSeq 500 machine (Illumina; up to 77 cycles—single end) and aligned to the human reference genome (GRCh38/hg38) using Bowtie2 (version 2.2.4 or 2.3.4.1; Langmead and Salzberg, 2012). Duplicate reads were marked with BamUtil (version 1.0.3; Jun et al., 2015) or Samtools markdup (version 1.9; Danecek et al., 2021). Resulting aligned read data were input for copy number calling using the Aneufinder R package (https://github.com/ataudt/aneufinder; Bakker et al., 2016). GC correction was performed and artifact-prone regions (known regions of extremely high or low coverage) were blacklisted. Libraries were analyzed using the dnacopy and edivisive copy number calling algorithms with variable width bins (average bin size 1 Mb, step size 500 kb). Libraries with an average of <10 reads per bin were discarded. Additionally, results for single-cell sequencing were curated by requiring a minimum concordance of 90% between the output of the two algorithms.

Immunoblotting

Protein extracts were obtained from cell pellets after lysis with high salt lysis buffer (20 mM Tris-HCl, pH 7.6, 300 mM NaCl, 10% glycerol, 0.2% [vol/vol] Igepal [cat. CA 630; Sigma-Aldrich]), processed in a Bioruptor sonicator (Diagenode), BCA (bicinchoninic acid) assay quantified, and denaturated at 95°C in 1X Laemmli sample buffer for 5 min. Samples were loaded on a polyacrylamide gel (BioRad) and transferred to a 0.45 μm nitrocellulose membrane (BioRad). ChemIluminescent signal (ECL generated) was acquired on a ChemiDoc imaging system (BioRad). Colorimetric images of relative nitrocellulose membrane were also acquired. Images were visualized and exported using Image Lab software (BioRad).The following antibodies were used for immunoblotting: DNMT1 (1:1,000, #5032, RRID:AB_10548197; Cell Signaling Technology); DNMT3B (1:1,000, #67259, RRID: AB_2799723; Cell Signaling Technology); DNM3A (1:2,000, ab188470, RRID: AB_3073896; Abcam); VINCULIN (1:5,000, V9264, RRID: AB_10603627; Sigma-Aldrich); p53 (1:200, OP43, RRID:AB_10683504; Merck); p21 (1:200, OP64, RRID:AB_2335868; Merck); and p16 (1:1,000, #92803, RRID:AB_2750891; Cell Signaling Technology).

Immunofluorescence and live-cell imaging

Cells were grown on poly-*L*-lysine–coated coverslips and fixed in PBS containing 4% formaldehyde and 0.1% Triton X-100 at room temperature for 10 min. Blocking was performed with 5% bovine serum albumin in 0.1% Tween-20 in PBS for 10 min or in 2.5% FBS (vol/vol), 0.2 M glycine, 0.1% triton X-100 (vol/vol) in PBS for 30 min at room temperature. Primary antibodies were incubated in blocking buffer for 1 h at room temperature. After washing with PBS 0.1% Triton X-100, coverslips were incubated with secondary antibodies conjugated to fluorochromes (Jackson Immuno Research) for 45 min at room temperature. The following antibodies were used: mNeonGreen (1:500; 32f6, RRID: AB_2827566; Chromotek). Coverslips were mounted using antifade reagent Prolong Gold containing DAPI (Life Technologies). Images were acquired on a DeltaVision Core system (Applied Precision) with 60X Olympus UPlanSApo oil-immersion objective (NA 1.4), 250 W Xenon light source equipped with a Photometrics CoolSNAP_HQ2 Camera. 4-μm Z-stacks were acquired (Z step size: 0.2 μm). Images from Z-stacks were projected and deconvolved using the softWoRx software.

For 5mC staining, cells were washed with 0.1% Tween-20 in PBS and fixed for 10 min in freshly prepared 4% formaldehyde in PBS. Cells were permeabilized with 0.5% Triton X-100 in PBS for 30 min and treated with 2 M HCl for 30 min at 25°C. After extensive wash with 0.1% Tween-20 in PBS, cells were blocked for 1 h in 2% BSA in 0.1% Tween-20 in PBS and then incubated anti-5mC antibody (1:500; A-1014; Epigentek, RRID:AB_2819207) in 0.1% Tween-20 in PBS overnight at 4°C and subsequently, after washing, with anti-mouse Alexa Fluor 647–conjugated secondary antibody (1:500; Cat# 715-605-150; Jackson ImmunoResearch Labs, RRID:AB_2340862) in 0.1% Tween-20 in PBS for 1 h at 37°C. DNA was stained with DAPI (1 μg/ml) for 5 min at room temperature and cells were imaged with a DeltaVision Core system (Applied Precision). Images from Z-stacks were projected and deconvolved using the softWoRx software.

For the live-cell imaging, cells were plated on high-optical quality plastic slides (Ibidi) treated 1 h before filming with SiR-DNA (1:1,000, SC007; Spirochrome) and imaged using a Deltavision Core system (Applied Precision).

Image quantification

Immunofluorescence signals were quantified by using FIJI software. A mask of the nuclei was obtained by thresholding the DAPI channel, and individual nuclei were detected using the Analyze Particles function. Five 15 × 15-pixel circles were drawn outside the nuclei (marked by DAPI staining) and the mean of the integrated signal was calculated (background). The integrated signal intensity of each individual nucleus was then calculated by subtracting the background.

Hybrid microscopy-cytometry (Imagestream) analysis

Cells were collected, counted, and fixed in 1% formaldehyde 20 min on ice. The reaction was blocked with the final 125 mM Glycine for 3 min. After washes with 1X PBS, cells were permeabilized with 1X permeabilization buffer (PB) (kit Foxp3/Transcription Factor Staining Buffer kit, 00-5523; Thermo Fisher Scientific) for 30 min at room temperature. Cells were resuspended in 1X PB containing H3K9me3 (1:700, ab8898, RRID:AB_306848; Abcam) or H3K27me3 (1:700, 9733S, RRID: AB_2616029; Cell Signaling Technology) antibodies and incubated for 1 h at room temperature.

After three washes in 1X PB, cells were resuspended in PB with anti-rabbit Alexa Fluor-647 conjugated secondary antibody (1:500; Cat# 711-605-152, RRID:AB_2492288; Jackson ImmunoResearch Labs) for 30 min, at room temperature. Following 2 washes in 1X PB, cells were resuspended cells in 30 µl of 1X FACS buffer (1% BSA, 2 mM EDTA in PBS) + PI (10 µg/ml) and acquired on an Amnis ImageStreamX MKII device set with proper compensation and unstained controls. Lasers 405 nm (70 mW), 488 nm (100 mW), 561 nm (50 mW), and 642 nm (50 mW) were used and parameters were recorded with INSPIRE software as follows: channels 01 and 09 for Brightfields (Ch01 and Ch09 BF), channel 02 for GFP (Ch02 GFP), channel 04 for PI (Ch04 PI), channel 07 for CFP (Ch07 CFP), and channel 11 for H3K9me3 or H3K27me3 AF647 (Ch11 AF647). Data analysis was performed with IDEAS software (V6.2). Cells in focus were selected based on the Gradient RMS feature on Ch01, then singlets were isolated using area and aspect ratio intensity features on Ch01. GFP positive and negative events were separated using Ch02 intensity, independently from CFP intensity. To focus on PI signal localization in the nucleus, three other specific masks were generated: Erode(M04, 4), consisting of eroding four pixels of the regular M04 mask, Dilate(M04, 1) to dilate of 1 pixel of the M04, and the combined mask: Dilate(M04, 1) and Not Erode(M04, 4). The Erode(M04, 4) represented the inner part of the nucleus when the Dilate(M04, 1), but not Erode(M04, 4), showed the nuclear membrane. Those masks were applied to an intensity feature, allowing the exclusion of outliers. To better assess the localization, an intensity ratio (ratio membrane/intra) was then created by dividing the intensity at the membrane by the intensity at the internal nuclear part. Nuclear (<1 "internal") and membrane (>1 "external") PI were separated at a ratio of 1.

MeDIP and real-time quantitative PCR (qPCR)

This method allows studies about DNA modifications and was performed as in Vella et al. (2013). Briefly, 1 µg of denatured and sonicated genomic DNA was immunoprecipitated overnight with 1 µg of rabbit anti 5mC antibody in 100 µl of IP buffer (10 mM Na-Phosphate, pH 7, 140 mM NaCl, 0,05% TritonX-100). Then, samples were incubated with 10 µl of Dynabeads protein A beads for 2 h (10001D; Thermo Fisher Scientific), washed four times with IP buffer, and bound DNA eluted by incubation with 20 µg proteinase K (Roche) at 50°C in proper digestion buffer. Eluted DNA was recovered and purified using QIAquick PCR purification kit (Qiagen). DNAme on specific TSSs were analyzed by qPCR using the primer pairs listed in Table S1.

MS-based 5mC quantification

Genomic DNA was extracted from cells using a NucleoSpin Tissue kit (740952; Macherey-Nagel), and 1 µg DNA was digested with Nucleoside Digestion Mix (M0649S; NEB) prior to MS. Analysis of total 5-mdC (5-methyl-2'-deoxycytidine) concentrations was performed using a Q Exactive mass spectrometer (Thermo Fisher Scientific). The instrument was equipped with an electrospray ionization source (H-ESI II Probe) coupled to an Ultimate 3000 RS HPLC (Thermo Fisher Scientific). A ThermoFisher Hypersil Gold aQ chromatography column (100 mm × 2.1 mm, 1.9-µm particle size) heated to 30°C was injected with digested DNA. The flow rate was set to 0.3 ml/min and the column was run for 10 min in isocratic eluent consisting of 1% acetonitrile in water containing 0.1% formic acid. Parent ions were fragmented in positive ion mode, parallel reaction monitoring mode at 10% normalized collision energy; MS2 resolution was 17,500, automatic gain control target was 2e5, maximum injection time was 50 ms, and separation window was 1.0 m/z. The inclusion list contained the following masses: dC (deoxycytidine) (228.1), 5-mdC (242.1). Extracted ion chromatograms (±5 ppm) of basic fragments were used for detection and quantification (dC: 112.0506 Da; 5-mdC: 126.0662 Da). Calibration curves were previously generated using synthetic standards in the ranges of 0.2–10 pmol injected for dC and 0.02–10 pmol for 5mdC. Results were expressed as % of total dC.

ELISA-based 5mC quantification

100 ng of genomic DNA was analyzed on a MethylFlash Global DNA Methylation (5-mC) ELISA Easy Kit (Colorimetric) (Epigentek, cat. P-1030) according to the manufacturer's instructions. 5mC levels were retrieved from OD and relative quantify was calculated relative to a standard curve. Results were expressed as 5mC % of total DNA.

COBRA

500 ng of genomic DNA was bisulfite converted with the EpiTect Fast 48 DNA Bisulfite Kit (Qiagen) according to the manufacturer's instructions. PCR amplification of converted DNA was performed with platinum Taq DNA polymerase (Thermo Fischer Scientific) and primer pairs (Table S1) with adjusted annealing temperatures. PCR amplicons were digested with 10 U BstUI (*TDRD6*, Alu), BstBI (Satellite II), HpyCH4IV (*GPT2*, *GPR119*) for 2 h at 65°C, 60°C, and 37°C, respectively. An equal amount of PCR product for the undigested control was used. Reactions were loaded onto a 3% agarose gel and visualized on a Chemidoc (BioRad). Bands were quantified by densitometry with ImageJ

and the percentage of methylated DNA was calculated over the total intensity of all the quantified bands.

5mC methylation array and analysis

Genomic DNA was extracted from cells using a NucleoSpin Tissue kit (740952; Macherey-Nagel) and DNA concentrations were determined in duplicate using the Quant-IT kit (Thermo Fisher Scientific). Samples with discordant results were verified in a second series of measurements. DNA quality and correspondence with sample characteristics were evaluated on a subset of the samples by migrating a small amount of DNA on a TapeStation 4200 (Agilent) to calculate the DNA Integrity number by a PCR amplification test (simultaneous amplification of two microsatellites markers) and a PCR-based verification of the sex of individuals. 1µg of genomic DNA was bisulfite converted with the EpiTect Fast 96 DNA Bisulfite Kit (Qiagen) according to the manufacturer's instructions. Genome-wide DNAme was analyzed on 850,000 CpGs with the Infinium Human MethylationEPIC Kit (Illumina) according to the manufacturer's instructions.

Raw data were extracted using the Bioconductor ChAMP package version 2.18 (Morris et al., 2014; Tian et al., 2017). All 16 samples were below the quality threshold of <10% of failed detection P value (>0.01) probes (global mean of 0.619% of failed probes) and no sample was therefore removed. Probes were further filtered as follows: detection P value > 0.01 (23,598 probes removed); beadcount <3 in at least 5% of samples (18,674 probes); non CpG probes (2,761 probes); and multihit probes as described in Nordlund et al. (2013) (8,375 probes).

Beta values, i.e., methylation level using the ratio of intensities between methylated and unmethylated alleles (between 0 and 1 with 0 being unmethylated and 1 fully methylated) were normalized using subset-quantile within array normalization (SWAN) normalization (Maksimovic et al., 2012).

DMPs between samples were obtained with Bioconductor ChAMP package function champ.DMP, which uses the limma package to calculate differential methylation probes between two phenotypes. To define DMP, a Δ of 0.3 of β-values median (interpreted as 30% methylation difference) with a P value <0.05 was set. P values were adjusted with the Benjamini–Hochberg method. Heat maps were generated on R software. As stated in the figure legends, heatmaps show a number of DMPs resulting from applying different Δβ values to accommodate a reasonable number of probes for graphic representation.

The different DMPs list of pairwise comparisons were annotated for gene locations according to Illumina annotation (promoter, TSS, gene body, 3′UTR, etc.). To discover the epigenetic context and the repetitive sequence feature of DMPs from pairwise comparisons, the Chromatin State Segmentation by HMM from ENCODE/Broad (Broad ChromHMM data [Ernst et al., 2011]) and Repeat Masker (Jurka, 2000) (https://www.repeatmasker.org), respectively, were exploited. Among the available ChromHMM datasets, the one relative to HepG2, having the most similar profile to DLD-1 cells, was used. Since the original fourth and fifth, sixth and seventh, 14th and 15th chromatin states are identical (namely, strong enhancers, weak enhancers, and repetitive/CNV, respectively), they were merged in our analysis for a total of 12 chromatin states. Statistical analyses were performed using the Chi-square test. Statistically changing categories, i.e., the ones contributing the most to the P values are indicated with "*" and assessed based on the standardized residuals, stdres > 2 calculated by R software).

Hi-C processing and data analysis

Hi-C assays were performed with an Arima Hi-C plus kit (#A510008; Arima Genomics) according to manufacturer's Instructions starting from 2*10^6 cells/reaction. Libraries preparations were performed with a Kapa Hyper Prep Kits with KAPA Library Amplification Primer Mix (07962347001; Roche), quantified by Qubit (Invitrogen), checked on a Tapestation device (Agilent) and pair-end sequenced on a NovaSeq platform (Illumina).

Hi-C data processing

Hi-C libraries were processed using the distiller pipeline (https://github.com/open2c/distiller-nf). Briefly, Hi-C sequencing reads were mapped to the hg38 assembly using bwa mem, and alignments were processed, deduplicated, and classified into contact pairs using pairtools (https://github.com/open2c/pairtools). Hi-C pairs were aggregated into multiresolution contact matrices, filtered, and normalized by iterative correction using the cooler package. Genome browser plots were generated using HiGlass and coolbox. Contact frequency versus distance profiles were calculated using cooltools.

IPG analysis

Spectral clustering and analysis were performed on Hi-C from untreated ^{NA}*DNMT1* cells using the inspectro package as described in Spracklin et al. (2023) applied to the first 10 eigenvectors of the contact matrix at 50-kb resolution. We compared the results of k-means with several functional and epigenomic tracks, including H3K9me3 and DNAme (this study), H3K27me3 and RNA-seq (Rokavec et al., 2017), as well as GC content and distance from centromere. Based on cluster metrics and interpretability, we selected k = 9 clusters and combined two pairs and one triplet of clusters whose functional profiles were largely similar but differed in overall proximity to the centromere to yield five IPGs. A comparison of IPGs with labels from SNIPER was generated using bioframe. Summaries of IPG-level observed/expected contact frequency were generated using cooltools.

ChIP

ChIP assays were carried out as in Scelfo et al. (2019) with minor modifications. Briefly, 1% formaldehyde crosslinked chromatin was resuspended in IP buffer (70 mM TRIS/HCl, pH 8.0, 5 mM EDTA, 100 mM NaCl, 0.3% SDS, 1.7% TRITON X-100), fragmented by sonication on ice (Branson sonicator Q700) to an average size of 300–600 bp and quantified by BCA method. 100 µg of sonicated chromatin was incubated overnight at 4°C with 2 µg of the indicated antibodies and recovered by Protein A-Sepharose 4B beads (101041; Thermo Fisher Scientific). DNA from washed beads was column-purified, quantified using the Qubit dsDNA HS, and used for library preparation at I. Curie genomic platform. For ChIP-qPCR analysis, the enrichment at

selected genomic loci (primer list, Table S1) was tested using LightCycler 480 SYBR Green I Master mix (04887352001; Roche) on a QuantStudio thermal cycler (Applied Biosystem).

ChIP-seq and RNA-seq data processing

ChIP-seq data, including data from Rokavec et al. (2017) were processed following the steps of the ENCODE ChIP-seq pipeline (https://github.com/ENCODE-DCC/chip-seq-pipeline2) with slight modifications using a simplified custom snakemake workflow as described in Spracklin et al. (2023). ChIP-seq tracks were compared by aggregating bigwig signal at 10-kb resolution using pybbi and generating density scatter plots using the matplotlib extension for datashader. RNA-seq data from Rokavec et al. (2017) was processed with the nf-core RNA-seq pipeline using default parameters.

Statistical analysis

Unless specified otherwise in the figure legends, statistical analyses were performed using Prism V9 software (Graphpad) or R software. Statistical significance of comparisons between two groups or experimental conditions were mainly assessed by two-tailed unpaired Student's *t* test. Data distribution was assumed to be normal, but this was not formally tested. Differences were considered significant if the computed P value was < 0.05. P values summary were defined as follows: *P < 0.05; **P < 0.01; ***P < 0.001; ****P < 0.0001; ns = not significant. Specialized statistical analyses pertaining to specific methods are fully described in the corresponding Materials and methods section.

Online supplemental material

Fig. S1 (related to Fig. 1) shows the characterization of the inducible DNMT1 degradation system established in RPE-1 cells. Fig. S2 (related to Fig. 2) displays additional characterization of global and locus-specific DNA demethylation upon IAA-induced DNMT1 degradation. Fig. S3 (related to Fig. 2) elucidates the DNMTA-independent locus-specific hypermethylation observed in the *DNMT3B* KO cells along with functional annotation of differentially methylated probes between selected experimental conditions. Fig. S4 (related to Fig. 3) shows additional data about cellular proliferation upon DNMTs degradation along with a correlation analysis between drug-induced methylation levels and relative cytotoxic effects. Fig. S5 (related to Fig. 4) provides further analyses and characterization of chromatin subcompartments and relative epigenetic patterns described in this demethylation system. Table S1 is a spreadsheet file listing the primers used in the work. Table S2 is a spreadsheet file reporting the number of significant differentially methylated probes identified between the experimental conditions analyzed in this work.

Data availability

Sequencing data generated in this work are deposited in the Gene Expression Omnibus database repository under the accession number GSE251935. The data underlying all figures and tables are available in the published article and its online supplemental material. Reagents and cell lines generated in this work will be shared upon reasonable formal request to the main corresponding author, Daniele Fachinetti (daniele.fachinetti@curie.fr).

Acknowledgments

We thank all the members of the Daniele Fachinetti team for the discussion and Edith Pfister (UMass Chan Medical School, Worcester, MA, USA) for editing the manuscript. We thank Hélöise Muller from Ines Drinnenberg's laboratory (Institut Curie, Paris, France) for advice and sharing reagents. We also acknowledge the Flow Cytometry Core Facility and the Cell and Tissue Imaging Facility (member of the French National Research Infrastructure France-BioImaging ANR10-INBS-04) of the Institut Curie and the DIMONEHEALT2019 equipment grant (project EpiK to Paola Arimondo).

D. Fachinetti receives salary support from the Centre National de la Recherche Scientifique and has received support for this project by Centre National de la Recherche Scientifique, Institut Curie, and Fondation ARC pour la recherche sur le cancer "ARC labellisation program 2019". A. Scelfo was supported by AIRC and from the European Union's Horizon 2020 research and innovation program under the Marie Skłodowska-Curie grant agreement No. 800924.

Author contributions: A. Scelfo., V. Barra, C. Salinas-Luypaert, and E. Bonaiti obtained the experimental data; V. Barra generated the cell lines; N. Abdennur and G. Spracklin performed the Hi-C analysis under the supervision of L. Mirny; F. Busato and J. Tost performed the methylation array analysis; G. Velasco provided technical and analysis expertise supervised by C. Francastel; A. Chipont performed the ImageStream data analysis under the supervision of C. Guérin; F. Bonhomme performed the LC-MS–based 5mC quantifications under the supervision of P. Arimondo; A.E. Tijhuis and D.C.J. Spierings performed the scWGS data acquisition and analysis under the supervision of F. Foijer; A. Scelfo, G. Spracklin, N. Abdennur, F. Busato, L. Mirny, and D. Fachinetti interpreted the results. A. Scelfo, G. Spracklin, N. Abdennur, L. Mirny, and D. Fachinetti designed the experiments. D. Fachinetti conceptualized the project and supervised the experimental work. D. Fachinetti, L. Mirny, J. Tost, C. Francastel, C. Guérin, and F. Foijer obtained funding. A. Scelfo and D. Fachinetti drafted the manuscript with input from N. Abdennur, G. Spracklin, and L. Mirny. All authors participated in reviewing and editing the manuscript.

Disclosures: J. Tost reported grants from the European Union, Agence National de Recherche, Fondation pour la Recherche Medicale, DBV Technologies, Anses, and UCB Pharma outside the submitted work. No other disclosures were reported.

Submitted: 6 July 2023
Revised: 20 November 2023
Accepted: 15 January 2024

References

Arand, J., D. Spieler, T. Karius, M.R. Branco, D. Meilinger, A. Meissner, T. Jenuwein, G. Xu, H. Leonhardt, V. Wolf, and J. Walter. 2012. In vivo control of CpG and non-CpG DNA methylation by DNA methyltransferases. *PLoS Genet.* 8:e1002750. https://doi.org/10.1371/journal.pgen.1002750

Bakker, B., A. Taudt, M.E. Belderbos, D. Porubsky, D.C. Spierings, T.V. de Jong, N. Halsema, H.G. Kazemier, K. Hoekstra-Wakker, A. Bradley, et al. 2016. Single-cell sequencing reveals karyotype heterogeneity in murine

and human malignancies. *Genome Biol.* 17:115. https://doi.org/10.1186/s13059-016-0971-7

Besselink, N., J. Keijer, C. Vermeulen, S. Boymans, J. de Ridder, A. van Hoeck, E. Cuppen, and E. Kuijk. 2023. The genome-wide mutational consequences of DNA hypomethylation. *Sci. Rep.* 13:6874. https://doi.org/10.1038/s41598-023-33932-3

Bestor, T.H., J.R. Edwards, and M. Boulard. 2015. Notes on the role of dynamic DNA methylation in mammalian development. *Proc. Natl. Acad. Sci. USA.* 112:6796–6799. https://doi.org/10.1073/pnas.1415301111

Bird, A.P. 1986. CpG-rich islands and the function of DNA methylation. *Nature.* 321:209–213. https://doi.org/10.1038/321209a0

Breiling, A., and F. Lyko. 2015. Epigenetic regulatory functions of DNA modifications: 5-methylcytosine and beyond. *Epigenetics Chromatin.* 8: 24. https://doi.org/10.1186/s13072-015-0016-6

Cai, Y., H.C. Tsai, R.C. Yen, Y.W. Zhang, X. Kong, W. Wang, L. Xia, and S.B. Baylin. 2017. Critical threshold levels of DNA methyltransferase 1 are required to maintain DNA methylation across the genome in human cancer cells. *Genome Res.* 27:533–544. https://doi.org/10.1101/gr.208108.116

Carollo, P.S., and V. Barra. 2023. Chromatin epigenetics and nuclear lamina keep the nucleus in shape: Examples from natural and accelerated aging. *Biol. Cell.* 115:e2200023. https://doi.org/10.1111/boc.202200023

Chen, T., S. Hevi, F. Gay, N. Tsujimoto, T. He, B. Zhang, Y. Ueda, and E. Li. 2007. Complete inactivation of DNMT1 leads to mitotic catastrophe in human cancer cells. *Nat. Genet.* 39:391–396. https://doi.org/10.1038/ng1982

Chen, Z.X., and A.D. Riggs. 2011. DNA methylation and demethylation in mammals. *J. Biol. Chem.* 286:18347–18353. https://doi.org/10.1074/jbc.R110.205286

Choudhury, S.R., Y. Cui, K. Lubecka, B. Stefanska, and J. Irudayaraj. 2016. CRISPR-dCas9 mediated TET1 targeting for selective DNA demethylation at BRCA1 promoter. *Oncotarget.* 7:46545–46556. https://doi.org/10.18632/oncotarget.10234

Choy, J.S., S. Wei, J.Y. Lee, S. Tan, S. Chu, and T.H. Lee. 2010. DNA methylation increases nucleosome compaction and rigidity. *J. Am. Chem. Soc.* 132:1782–1783. https://doi.org/10.1021/ja910264z

Danecek, P., J.K. Bonfield, J. Liddle, J. Marshall, V. Ohan, M.O. Pollard, A. Whitwham, T. Keane, S.A. McCarthy, R.M. Davies, and H. Li. 2021. Twelve years of SAMtools and BCFtools. *Gigascience.* 10:giab008. https://doi.org/10.1093/gigascience/giab008

Du, Q., G.C. Smith, P.L. Luu, J.M. Ferguson, N.J. Armstrong, C.E. Caldon, E.M. Campbell, S.S. Nair, E. Zotenko, C.M. Gould, et al. 2021. DNA methylation is required to maintain both DNA replication timing precision and 3D genome organization integrity. *Cell Rep.* 36:109722. https://doi.org/10.1016/j.celrep.2021.109722

Egger, G., S. Jeong, S.G. Escobar, C.C. Cortez, T.W. Li, Y. Saito, C.B. Yoo, P.A. Jones, and G. Liang. 2006. Identification of DNMT1 (DNA methyltransferase 1) hypomorphs in somatic knockouts suggests an essential role for DNMT1 in cell survival. *Proc. Natl. Acad. Sci. USA.* 103: 14080–14085. https://doi.org/10.1073/pnas.0604602103

Ernst, J., and M. Kellis. 2017. Chromatin-state discovery and genome annotation with ChromHMM. *Nat. Protoc.* 12:2478–2492. https://doi.org/10.1038/nprot.2017.124

Ernst, J., P. Kheradpour, T.S. Mikkelsen, N. Shoresh, L.D. Ward, C.B. Epstein, X. Zhang, L. Wang, R. Issner, M. Coyne, et al. 2011. Mapping and analysis of chromatin state dynamics in nine human cell types. *Nature.* 473:43–49. https://doi.org/10.1038/nature09906

Fatemi, M., A. Hermann, H. Gowher, and A. Jeltsch. 2002. Dnmt3a and Dnmt1 functionally cooperate during de novo methylation of DNA. *Eur. J. Biochem.* 269:4981–4984. https://doi.org/10.1046/j.1432-1033.2002.03198.x

Fatemi, M., A. Hermann, S. Pradhan, and A. Jeltsch. 2001. The activity of the murine DNA methyltransferase Dnmt1 is controlled by interaction of the catalytic domain with the N-terminal part of the enzyme leading to an allosteric activation of the enzyme after binding to methylated DNA. *J. Mol. Biol.* 309:1189–1199. https://doi.org/10.1006/jmbi.2001.4709

Feinberg, A.P., and B. Vogelstein. 1983. Hypomethylation distinguishes genes of some human cancers from their normal counterparts. *Nature.* 301: 89–92. https://doi.org/10.1038/301089a0

Fu, K., G. Bonora, and M. Pellegrini. 2020. Interactions between core histone marks and DNA methyltransferases predict DNA methylation patterns observed in human cells and tissues. *Epigenetics.* 15:272–282. https://doi.org/10.1080/15592294.2019.1666649

Gilbert, N., I. Thomson, S. Boyle, J. Allan, B. Ramsahoye, and W.A. Bickmore. 2007. DNA methylation affects nuclear organization, histone modifications, and linker histone binding but not chromatin compaction. *J. Cell Biol.* 177: 401–411. https://doi.org/10.1083/jcb.200607133

Grandjean, V., R. Yaman, F. Cuzin, and M. Rassoulzadegan. 2007. Inheritance of an epigenetic mark: The CpG DNA methyltransferase 1 is required for de novo establishment of a complex pattern of non-CpG methylation. *PLoS One.* 2:e1136. https://doi.org/10.1371/journal.pone.0001136

Greenberg, M.V.C., and D. Bourc'his. 2019. The diverse roles of DNA methylation in mammalian development and disease. *Nat. Rev. Mol. Cell Biol.* 20:590–607. https://doi.org/10.1038/s41580-019-0159-6

Haggerty, C., H. Kretzmer, C. Riemenschneider, A.S. Kumar, A.L. Mattei, N. Bailly, J. Gottfreund, P. Giesselmann, R. Weigert, B. Brändl, et al. 2021. Dnmt1 has de novo activity targeted to transposable elements. *Nat. Struct. Mol. Biol.* 28:594–603. https://doi.org/10.1038/s41594-021-00603-8

Hansen, R.S., C. Wijmenga, P. Luo, A.M. Stanek, T.K. Canfield, C.M. Weemaes, and S.M. Gartler. 1999. The DNMT3B DNA methyltransferase gene is mutated in the ICF immunodeficiency syndrome. *Proc. Natl. Acad. Sci. USA.* 96:14412–14417. https://doi.org/10.1073/pnas.96.25.14412

Hervouet, E., P. Peixoto, R. Delage-Mourroux, M. Boyer-Guittaut, and P.F. Cartron. 2018. Specific or not specific recruitment of DNMTs for DNA methylation, an epigenetic dilemma. *Clin. Epigenetics.* 10:17. https://doi.org/10.1186/s13148-018-0450-y

Hoffmann, S., and D. Fachinetti. 2018. Real-time de novo deposition of centromeric histone-associated proteins using the auxin-inducible degradation system. *Methods Mol. Biol.* 1832:223–241. https://doi.org/10.1007/978-1-4939-8663-7_12

Holland, A.J., D. Fachinetti, J.S. Han, and D.W. Cleveland. 2012. Inducible, reversible system for the rapid and complete degradation of proteins in mammalian cells. *Proc. Natl. Acad. Sci. USA.* 109:E3350–E3357. https://doi.org/10.1073/pnas.1216880109

Hotchkiss, R.D. 1948. The quantitative separation of purines, pyrimidines, and nucleosides by paper chromatography. *J. Biol. Chem.* 175:315–332. https://doi.org/10.1016/S0021-9258(18)57261-6

Imakaev, M., G. Fudenberg, R.P. McCord, N. Naumova, A. Goloborodko, B.R. Lajoie, J. Dekker, and L.A. Mirny. 2012. Iterative correction of Hi-C data reveals hallmarks of chromosome organization. *Nat. Methods.* 9: 999–1003. https://doi.org/10.1038/nmeth.2148

Ito, S., L. Shen, Q. Dai, S.C. Wu, L.B. Collins, J.A. Swenberg, C. He, and Y. Zhang. 2011. Tet proteins can convert 5-methylcytosine to 5-formylcytosine and 5-carboxylcytosine. *Science.* 333:1300–1303. https://doi.org/10.1126/science.1210597

Jackson-Grusby, L., C. Beard, R. Possemato, M. Tudor, D. Fambrough, G. Csankovszki, J. Dausman, P. Lee, C. Wilson, E. Lander, and R. Jaenisch. 2001. Loss of genomic methylation causes p53-dependent apoptosis and epigenetic deregulation. *Nat. Genet.* 27:31–39. https://doi.org/10.1038/83730

Jair, K.W., K.E. Bachman, H. Suzuki, A.H. Ting, I. Rhee, R.W. Yen, S.B. Baylin, and K.E. Schuebel. 2006. De novo CpG island methylation in human cancer cells. *Cancer Res.* 66:682–692. https://doi.org/10.1158/0008-5472.CAN-05-1980

Jin, B., Y. Li, and K.D. Robertson. 2011. DNA methylation: Superior or subordinate in the epigenetic hierarchy? *Genes Cancer.* 2:607–617. https://doi.org/10.1177/1947601910393957

Jones, P.A. 2012. Functions of DNA methylation: Islands, start sites, gene bodies and beyond. *Nat. Rev. Genet.* 13:484–492. https://doi.org/10.1038/nrg3230

Jun, G., M.K. Wing, G.R. Abecasis, and H.M. Kang. 2015. An efficient and scalable analysis framework for variant extraction and refinement from population-scale DNA sequence data. *Genome Res.* 25:918–925. https://doi.org/10.1101/gr.176552.114

Jurka, J. 2000. Repbase update: A database and an electronic journal of repetitive elements. *Trends Genet.* 16:418–420. https://doi.org/10.1016/S0168-9525(00)02093-X

Jüttermann, R., E. Li, and R. Jaenisch. 1994. Toxicity of 5-aza-2′-deoxycytidine to mammalian cells is mediated primarily by covalent trapping of DNA methyltransferase rather than DNA demethylation. *Proc. Natl. Acad. Sci. USA.* 91:11797–11801. https://doi.org/10.1073/pnas.91.25.11797

Kikuchi, A., H. Onoda, K. Yamaguchi, S. Kori, S. Matsuzawa, Y. Chiba, S. Tanimoto, S. Yoshimi, H. Sato, A. Yamagata, et al. 2022. Structural basis for activation of DNMT1. *Nat. Commun.* 13:7130. https://doi.org/10.1038/s41467-022-34779-4

Langmead, B., and S.L. Salzberg. 2012. Fast gapped-read alignment with Bowtie 2. *Nat. Methods.* 9:357–359. https://doi.org/10.1038/nmeth.1923

Lehnertz, B., Y. Ueda, A.A. Derijck, U. Braunschweig, L. Perez-Burgos, S. Kubicek, T. Chen, E. Li, T. Jenuwein, and A.H. Peters. 2003. Suv39h-

mediated histone H3 lysine 9 methylation directs DNA methylation to major satellite repeats at pericentric heterochromatin. *Curr. Biol.* 13: 1192–1200. https://doi.org/10.1016/S0960-9822(03)00432-9

Liang, G., M.F. Chan, Y. Tomigahara, Y.C. Tsai, F.A. Gonzales, E. Li, P.W. Laird, and P.A. Jones. 2002. Cooperativity between DNA methyltransferases in the maintenance methylation of repetitive elements. *Mol. Cell. Biol.* 22: 480–491. https://doi.org/10.1128/MCB.22.2.480-491.2002

Lieberman-Aiden, E., N.L. van Berkum, L. Williams, M. Imakaev, T. Ragoczy, A. Telling, I. Amit, B.R. Lajoie, P.J. Sabo, M.O. Dorschner, et al. 2009. Comprehensive mapping of long-range interactions reveals folding principles of the human genome. *Science*. 326:289–293. https://doi.org/10.1126/science.1181369

Liu, X.S., H. Wu, X. Ji, Y. Stelzer, X. Wu, S. Czauderna, J. Shu, D. Dadon, R.A. Young, and R. Jaenisch. 2016. Editing DNA methylation in the mammalian genome. *Cell*. 167:233–247.e17. https://doi.org/10.1016/j.cell.2016.08.056

Liu, Y., and W.F. Bodmer. 2006. Analysis of P53 mutations and their expression in 56 colorectal cancer cell lines. *Proc. Natl. Acad. Sci. USA*. 103: 976–981. https://doi.org/10.1073/pnas.0510146103

Loonstra, A., M. Vooijs, H.B. Beverloo, B.A. Allak, E. van Drunen, R. Kanaar, A. Berns, and J. Jonkers. 2001. Growth inhibition and DNA damage induced by Cre recombinase in mammalian cells. *Proc. Natl. Acad. Sci. USA*. 98:9209–9214. https://doi.org/10.1073/pnas.161269798

Maksimovic, J., L. Gordon, and A. Oshlack. 2012. SWAN: Subset-quantile within array normalization for illumina infinium HumanMethylation450 BeadChips. *Genome Biol.* 13:R44. https://doi.org/10.1186/gb-2012-13-6-r44

Matarazzo, M.R., S. Boyle, M. D'Esposito, and W.A. Bickmore. 2007. Chromosome territory reorganization in a human disease with altered DNA methylation. *Proc. Natl. Acad. Sci. USA*. 104:16546–16551. https://doi.org/10.1073/pnas.0702924104

Meissner, A., T.S. Mikkelsen, H. Gu, M. Wernig, J. Hanna, A. Sivachenko, X. Zhang, B.E. Bernstein, C. Nusbaum, D.B. Jaffe, et al. 2008. Genome-scale DNA methylation maps of pluripotent and differentiated cells. *Nature*. 454:766–770. https://doi.org/10.1038/nature07107

Morris, T.J., L.M. Butcher, A. Feber, A.E. Teschendorff, A.R. Chakravarthy, T.K. Wojdacz, and S. Beck. 2014. ChAMP: 450k chip analysis methylation pipeline. *Bioinformatics*. 30:428–430. https://doi.org/10.1093/bioinformatics/btt684

Natsume, T., T. Kiyomitsu, Y. Saga, and M.T. Kanemaki. 2016. Rapid protein depletion in human cells by auxin-inducible degron tagging with short homology donors. *Cell Rep.* 15:210–218. https://doi.org/10.1016/j.celrep.2016.03.001

Nishimura, K., T. Fukagawa, H. Takisawa, T. Kakimoto, and M. Kanemaki. 2009. An auxin-based degron system for the rapid depletion of proteins in nonplant cells. *Nat. Methods*. 6:917–922. https://doi.org/10.1038/nmeth.1401

Nishiyama, A., and M. Nakanishi. 2021. Navigating the DNA methylation landscape of cancer. *Trends Genet.* 37:1012–1027. https://doi.org/10.1016/j.tig.2021.05.002

Nordlund, J., C.L. Bäcklin, P. Wahlberg, S. Busche, E.C. Berglund, M.L. Eloranta, T. Flaegstad, E. Forestier, B.M. Frost, A. Harila-Saari, et al. 2013. Genome-wide signatures of differential DNA methylation in pediatric acute lymphoblastic leukemia. *Genome Biol.* 14:r105. https://doi.org/10.1186/gb-2013-14-9-r105

Padeken, J., and P. Heun. 2014. Nucleolus and nuclear periphery: Velcro for heterochromatin. *Curr. Opin. Cell Biol.* 28:54–60. https://doi.org/10.1016/j.ceb.2014.03.001

Palii, S.S., B.O. Van Emburgh, U.T. Sankpal, K.D. Brown, and K.D. Robertson. 2008. DNA methylation inhibitor 5-Aza-2′-deoxycytidine induces reversible genome-wide DNA damage that is distinctly influenced by DNA methyltransferases 1 and 3B. *Mol. Cell. Biol.* 28:752–771. https://doi.org/10.1128/MCB.01799-07

Pappalardi, M.B., K. Keenan, M. Cockerill, W.A. Kellner, A. Stowell, C. Sherk, K. Wong, S. Pathuri, J. Briand, M. Steidel, et al. 2021. Discovery of a first-in-class reversible DNMT1-selective inhibitor with improved tolerability and efficacy in acute myeloid leukemia. *Nat. Cancer*. 2: 1002–1017. https://doi.org/10.1038/s43018-021-00249-x

Peters, S.L., R.A. Hlady, J. Opavska, D. Klinkebiel, S. Novakova, L.M. Smith, R.E. Lewis, A.R. Karpf, M.A. Simpson, L. Wu, and R. Opavsky. 2013. Essential role for Dnmt1 in the prevention and maintenance of MYC-induced T-cell lymphomas. *Mol. Cell. Biol.* 33:4321–4333. https://doi.org/10.1128/MCB.00776-13

Rao, S.S., M.H. Huntley, N.C. Durand, E.K. Stamenova, I.D. Bochkov, J.T. Robinson, A.L. Sanborn, I. Machol, A.D. Omer, E.S. Lander, and E.L. Aiden. 2014. A 3D map of the human genome at kilobase resolution reveals principles of chromatin looping. *Cell*. 159:1665–1680. https://doi.org/10.1016/j.cell.2014.11.021

Razin, A., and R. Shemer. 1995. DNA methylation in early development. *Hum. Mol. Genet.* 4:1751–1755. https://doi.org/10.1093/hmg/4.suppl_1.1751

Rhee, I., K.E. Bachman, B.H. Park, K.W. Jair, R.W. Yen, K.E. Schuebel, H. Cui, A.P. Feinberg, C. Lengauer, K.W. Kinzler, et al. 2002. DNMT1 and DNMT3b cooperate to silence genes in human cancer cells. *Nature*. 416: 552–556. https://doi.org/10.1038/416552a

Rhee, I., K.W. Jair, R.W. Yen, C. Lengauer, J.G. Herman, K.W. Kinzler, B. Vogelstein, S.B. Baylin, and K.E. Schuebel. 2000. CpG methylation is maintained in human cancer cells lacking DNMT1. *Nature*. 404: 1003–1007. https://doi.org/10.1038/35010000

Robertson, K.D. 2005. DNA methylation and human disease. *Nat. Rev. Genet.* 6:597–610. https://doi.org/10.1038/nrg1655

Rokavec, M., D. Horst, and H. Hermeking. 2017. Cellular model of colon cancer progression reveals signatures of mRNAs, miRNA, lncRNAs, and epigenetic modifications associated with metastasis. *Cancer Res.* 77: 1854–1867. https://doi.org/10.1158/0008-5472.CAN-16-3236

Rose, N.R., and R.J. Klose. 2014. Understanding the relationship between DNA methylation and histone lysine methylation. *Biochim. Biophys. Acta*. 1839:1362–1372. https://doi.org/10.1016/j.bbagrm.2014.02.007

Samanta, S., S. Rajasingh, T. Cao, B. Dawn, and J. Rajasingh. 2017. Epigenetic dysfunctional diseases and therapy for infection and inflammation. *Biochim. Biophys. Acta Mol. Basis Dis.* 1863:518–528. https://doi.org/10.1016/j.bbadis.2016.11.030

Sánchez, O.F., A. Mendonca, A. Min, J. Liu, and C. Yuan. 2019. Monitoring histone methylation (H3K9me3) changes in live cells. *ACS Omega*. 4: 13250–13259. https://doi.org/10.1021/acsomega.9b01413

Sapozhnikov, D.M., and M. Szyf. 2021. Unraveling the functional role of DNA demethylation at specific promoters by targeted steric blockage of DNA methyltransferase with CRISPR/dCas9. *Nat. Commun.* 12:5711. https://doi.org/10.1038/s41467-021-25991-9

Scelfo, A., D. Fernández-Pérez, S. Tamburri, M. Zanotti, E. Lavarone, M. Soldi, T. Bonaldi, K.J. Ferrari, and D. Pasini. 2019. Functional landscape of PCGF proteins reveals both RING1A/B-Dependent-and RING1A/B-Independent-Specific activities. *Mol. Cell*. 74:1037–1052.e7. https://doi.org/10.1016/j.molcel.2019.04.002

Schutsky, E.K., C.S. Nabel, A.K.F. Davis, J.E. DeNizio, and R.M. Kohli. 2017. APOBEC3A efficiently deaminates methylated, but not TET-oxidized, cytosine bases in DNA. *Nucleic Acids Res.* 45:7655–7665. https://doi.org/10.1093/nar/gkx345

Shen, L., H. Wu, D. Diep, S. Yamaguchi, A.C. D'Alessio, H.L. Fung, K. Zhang, and Y. Zhang. 2013. Genome-wide analysis reveals TET- and TDG-dependent 5-methylcytosine oxidation dynamics. *Cell*. 153:692–706. https://doi.org/10.1016/j.cell.2013.04.002

Slotkin, R.K., and R. Martienssen. 2007. Transposable elements and the epigenetic regulation of the genome. *Nat. Rev. Genet.* 8:272–285. https://doi.org/10.1038/nrg2072

Spada, F., A. Haemmer, D. Kuch, U. Rothbauer, L. Schermelleh, E. Kremmer, T. Carell, G. Längst, and H. Leonhardt. 2007. DNMT1 but not its interaction with the replication machinery is required for maintenance of DNA methylation in human cells. *J. Cell Biol.* 176:565–571. https://doi.org/10.1083/jcb.200610062

Spracklin, G., N. Abdennur, M. Imakaev, N. Chowdhury, S. Pradhan, L.A. Mirny, and J. Dekker. 2023. Diverse silent chromatin states modulate genome compartmentalization and loop extrusion barriers. *Nat. Struct. Mol. Biol.* 30:38–51. https://doi.org/10.1038/s41594-022-00892-7

Tian, Y., T.J. Morris, A.P. Webster, Z. Yang, S. Beck, A. Feber, and A.E. Teschendorff. 2017. ChAMP: Updated methylation analysis pipeline for illumina BeadChips. *Bioinformatics*. 33:3982–3984. https://doi.org/10.1093/bioinformatics/btx513

van den Bos, H., B. Bakker, A. Taudt, V. Guryev, M. Colomé-Tatché, P.M. Lansdorp, F. Foijer, and D.C.J. Spierings. 2019. Quantification of aneuploidy in mammalian systems. *Methods Mol. Biol.* 1896:159–190. https://doi.org/10.1007/978-1-4939-8931-7_15

Velasco, G., G. Grillo, N. Touleimat, L. Ferry, I. Ivkovic, F. Ribierre, J.F. Deleuze, S. Chantalat, C. Picard, and C. Francastel. 2018. Comparative methylome analysis of ICF patients identifies heterochromatin loci that require ZBTB24, CDCA7 and HELLS for their methylated state. *Hum. Mol. Genet.* 27:2409–2424. https://doi.org/10.1093/hmg/ddy130

Vella, P., A. Scelfo, S. Jammula, F. Chiacchiera, K. Williams, A. Cuomo, A. Roberto, J. Christensen, T. Bonaldi, K. Helin, and D. Pasini. 2013. Tet proteins connect the O-linked N-acetylglucosamine transferase Ogt to chromatin in embryonic stem cells. *Mol. Cell*. 49:645–656. https://doi.org/10.1016/j.molcel.2012.12.019

Vilkaitis, G., I. Suetake, S. Klimasauskas, and S. Tajima. 2005. Processive methylation of hemimethylated CpG sites by mouse Dnmt1 DNA methyltransferase. *J. Biol. Chem.* 280:64–72. https://doi.org/10.1074/jbc.M411126200

Walton, E.L., C. Francastel, and G. Velasco. 2011. Maintenance of DNA methylation: Dnmt3b joins the dance. *Epigenetics*. 6:1373–1377. https://doi.org/10.4161/epi.6.11.17978

Weber, M., J.J. Davies, D. Wittig, E.J. Oakeley, M. Haase, W.L. Lam, and D. Schübeler. 2005. Chromosome-wide and promoter-specific analyses identify sites of differential DNA methylation in normal and transformed human cells. *Nat. Genet.* 37:853–862. https://doi.org/10.1038/ng1598

Xiong, K., and J. Ma. 2019. Revealing Hi-C subcompartments by imputing inter-chromosomal chromatin interactions. *Nat. Commun.* 10:5069. https://doi.org/10.1038/s41467-019-12954-4

Xiong, Z., and P.W. Laird. 1997. COBRA: A sensitive and quantitative DNA methylation assay. *Nucleic Acids Res.* 25:2532–2534. https://doi.org/10.1093/nar/25.12.2532

Supplemental material

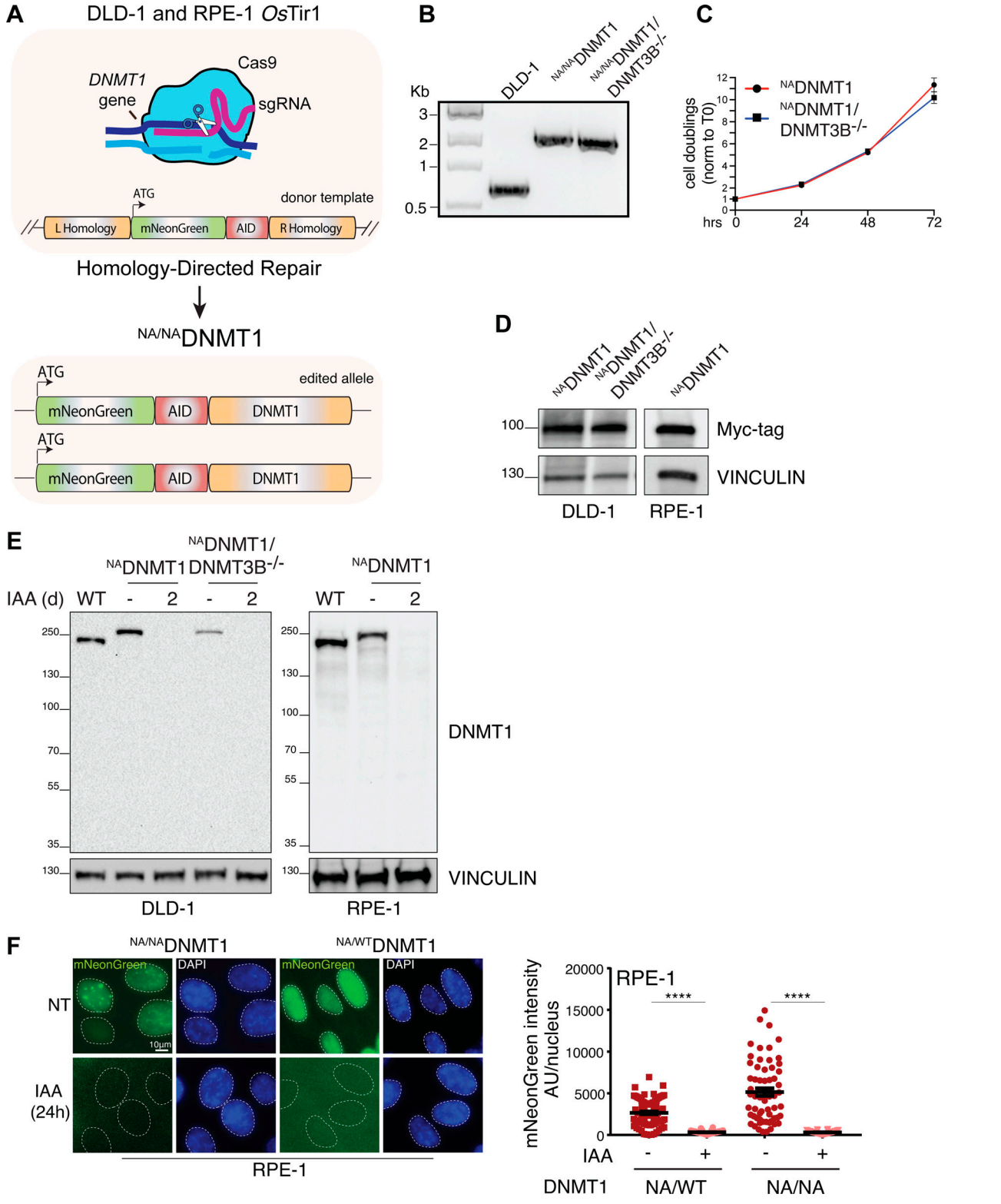

Figure S1. **Generation of an inducible DNMT1 degradation system. (A)** Schematics of the endogenous *DNMT1* gene tagging strategy by CRISPR/Cas9 approach. **(B)** Genotyping PCR on selected WT, ^{NA}*DNMT1*, and ^{NA}*DNMT1/DNMT3B*$^{-/-}$ clones showing homozygous tagging of *DNMT1* gene with the mNeonGreen-AID module. **(C)** Cell doubling measurement obtained from real-time cell index of the indicated DLD-1 cells. Values are normalized to time 0. **(D)** Immunoblot analysis showing Myc-tag OsTIR1 expression in the indicated cell lines. VINCULIN served as loading control. **(E)** Immunoblot analysis with the DNMT1 antibody of the indicated cell lines and treatment conditions. VINCULIN served as loading control. **(F)** Representative immunofluorescence images (left) and relative quantification (right) of mNeonGreen fluorescence signal in the indicated cell lines. IAA treatment: 24 h. NA/WT: heterozygous clone; NA/NA: homozygous clone. Each dot represents one analyzed nucleus (n > 60 for condition). Error bars represent the SEM. Unpaired t test: ****P < 0.0001. d, day. Source data are available for this figure: SourceData FS1.

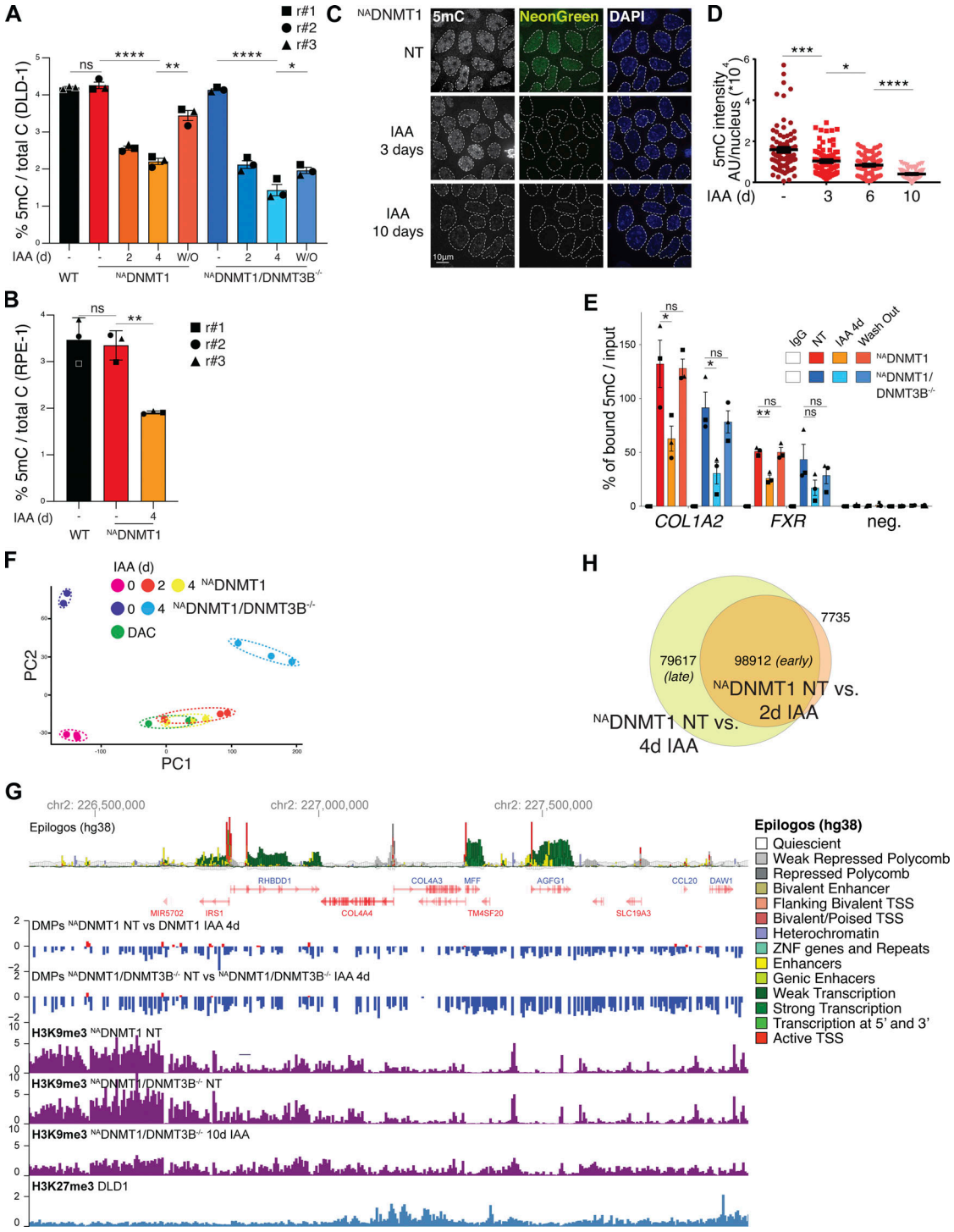

Figure S2. **Induced DNMT1 degradation leads to progressive DNA demethylation. (A)** Percentage of 5mC over total C quantified by LC-MS on DNA from the indicated DLD-1 cell lines and conditions. W/O: 4 days (d). Dots indicate independent experiments. *N* = 3. Error bars represent SEM. Unpaired *t* test: *P = 0.038; **P = 0.015; ****P < 0.0001. **(B)** Percentage of 5mC over total C quantified by LC-MS on DNA from the indicated RPE-1 cell lines and conditions. Dots indicate independent experiments. *N* = 3. Error bars represent SEM. Unpaired *t* test: **P = 0.014. **(C)** Representative immunofluorescence images of the indicated cell lines and treatment conditions with a 5mC antibody. mNeonGreen was used to detect DNMT1. Scale bar: 10 µm. **(D)** Quantification of 5mC nuclear signal at different times of IAA treatment of *NADNMT1* cells. Each dot corresponds to one analyzed nucleus (*n* > 74 for condition). Error bars represent SEM. Unpaired *t* test: *P = 0.0348, ***P = 0.002 ****P < 0.0001. **(E)** MeDIP analysis at selected promoter regions in the indicated cell lines and conditions. IgG served as isotype control. Each dot corresponds to the mean value of one replicate (*N* = 3), done in technical duplicate (*n* = 2). Error bars represent SEM. Unpaired *t* test. *P = 0.0495, 0.00257; **P = 0.0025. **(F)** PCA plot of DNAme variations among the indicated cell lines and treatment conditions. Biological replicates are represented by individual dots, same conditions are enclosed by a dashed ellipse. **(G)** Genomic snapshot of a region on chromosome 2 with different features (epilogos) showing: DMPs between the indicated conditions; H3K9me3 and H3K27me3 ChIP-seq profiles in the indicated cell lines. **(H)** Venn diagram indicating the numbers of common and unique DMPs (Δβ-value ≥ 30%) identified in the indicated comparisons.

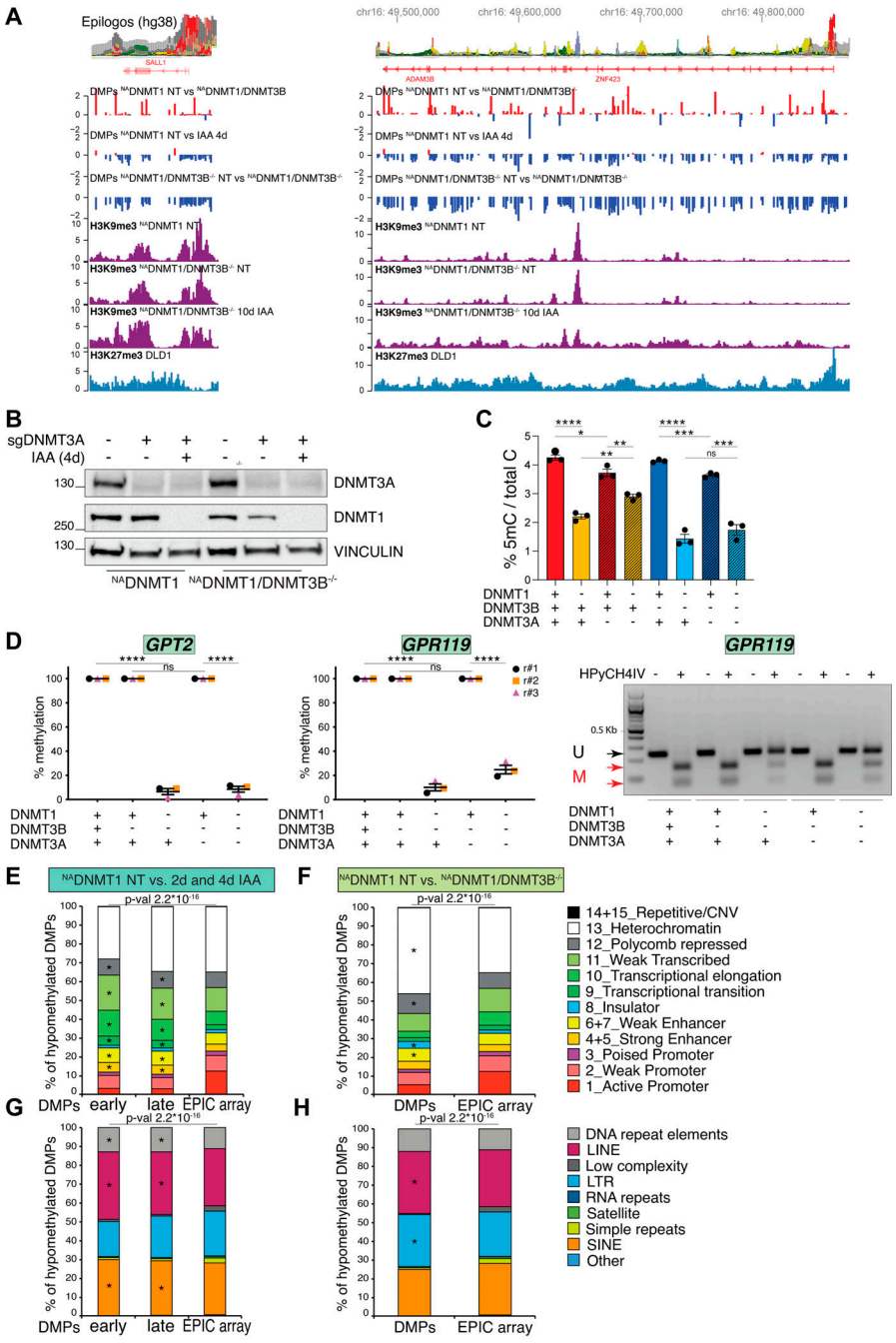

Figure S3. **DNMT3A-independent locus-specific hypermethylation in *DNMT3B* KO cells. (A)** Representative genomic snapshots showing hypermethylation of two regions on chromosome 16 with relative features (epilogos). The following profiles on the indicated cells are shown: DMPs between the indicated conditions; H3K9me3 and H3K27me3 ChIP-seq. **(B)** Immunoblot analysis of DNMT3A and DNMT3B levels on indicated cell lines and treatment conditions. VINCULIN served as loading control. *DNMT3A* KD was performed for 4 days (d). **(C)** Percentage of 5mC over total C quantified by LC-MS on DNA from the indicated DLD-1 cell lines and conditions. Dots indicate independent experiments. *N* = 3. Error bars represent SEM. Unpaired *t* test: *P = 0.0263, **P = 0.0031 and 0.0049, ***P = 0.0007 and 0.0005, ****P < 0.0001, ns = not significant. **(D)** Quantification of methylated DNA (as percentage of the total) at the indicated regions by COBRA assay normalized to relative untreated control. Each dot represents one biological replicate (*N* = 3); error bars represent the SEM. Unpaired *t* test: ****P < 0.0001. **(E and F)** Distribution of the indicated pairwise hypo-DMPs relative to the 15 chromatin states (ChromHMM from ENCODE, Hep2G cell line) compared with the distribution of all the probes present on the EPIC array. Since the originally described 4th and 5th, 6th and 7th, 14th and 15th chromatin states (strong enhancers, weak enhancers, and repetitive/CNV, respectively) are identical, they have been merged in our analysis for a total of 12 chromatin states. A chi-square test was used to calculate the P value and define significant changes in the distribution of DMPs of the indicated categories relative to EPIC array composition. Stars (*) indicate the chromatin states with a major change (i.e., contributing the most to the P value based on the standardized residuals, stdres > 2, calculated by R software). **(G and H)** Distribution of the indicated pairwise hypo-DMPs relative to the annotated DNA repeats (Repeat Masker) compared to the distribution of all the probes present on the EPIC array. A chi-square test was used to calculate P value and define significant changes in the distribution of DMPs of the indicated categories relative to EPIC array composition. Stars (*) indicate the categories with major change (i.e., contributing the most to the P value based on the standardized residuals, stdres > 2). Source data are available for this figure: SourceData FS3.

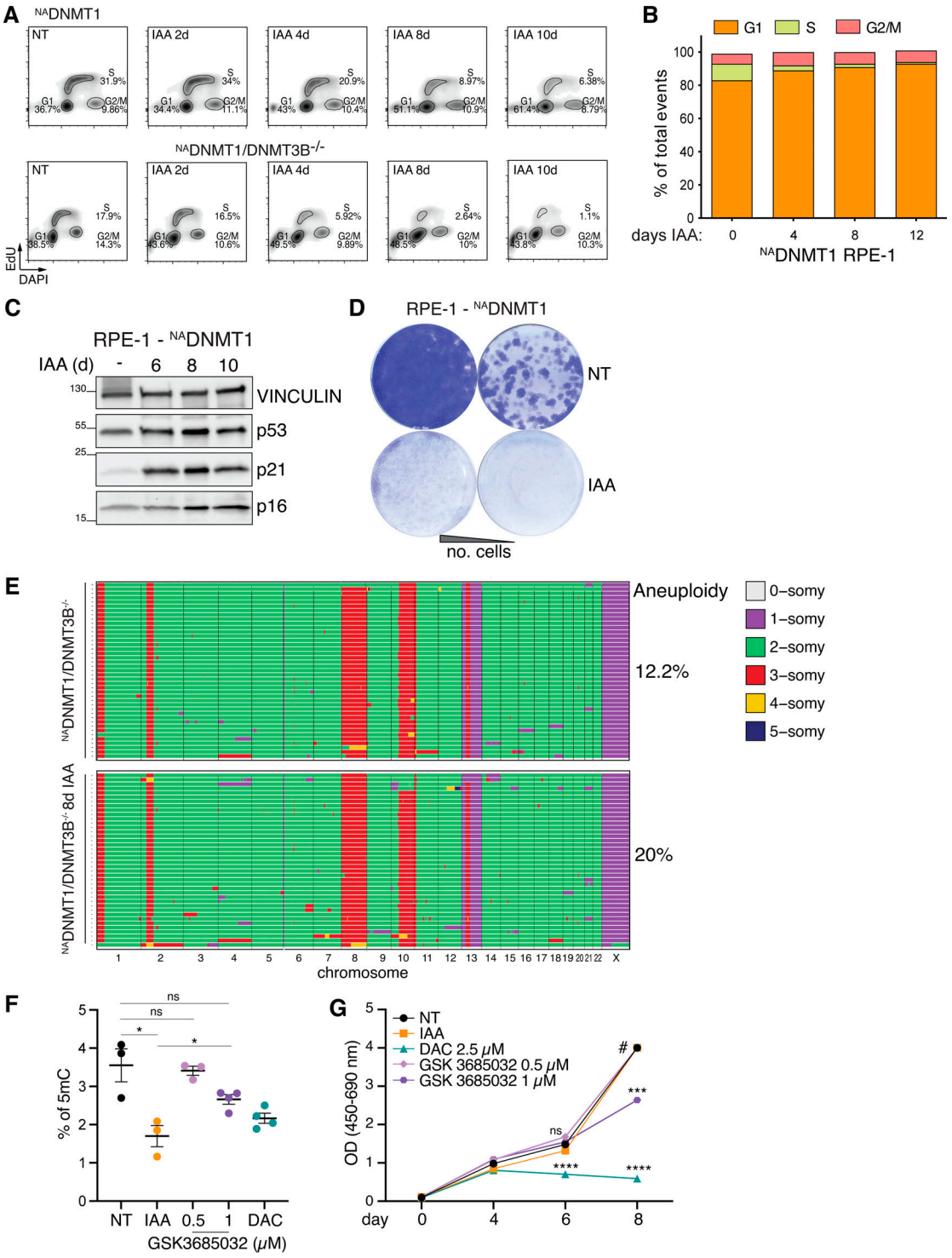

Figure S4. **DNMTs degradation impairs cell proliferation. (A)** Representative plot of cell cycle analysis of *NADNMT1* and *NADNMT1/DNMT3B*$^{-/-}$ DLD-1 cells upon IAA treatment for the indicated times. Shown gates were set with the auto-gating tool (FlowJo). **(B)** Quantification of cell cycle phases of the *NADNMT1* RPE-1 cells treated with IAA for the indicated times. **(C)** Immunoblot analysis with the indicated antibodies of cell extract from *NADNMT1* RPE-1 cells. VINCULIN served as loading control. d, day. **(D)** Representative images of colony formation assay of the *NADNMT1* RPE-1 cells treated with IAA for 12 days. **(E)** Single-cell whole-genome sequencing of *NADNMT1/DNMT3B*$^{-/-}$ treated cells as indicated (8 days IAA treatment). Each row represents an individual cell, and chromosomes are plotted as columns. Colors correspond to a defined copy-number state (legend on the right). The percentage of cells showing whole-chromosome aneuploidy (loss or gain, besides chromosomes 8 and 13) is also indicated. **(F)** Quantification of methylated DNA (as percentage of the total DNA) of *NADNMT1* DLD-1 cells treated for 6 days as indicated. DAC: 2.5 μM. Dots indicate independent experiments. $N > 3$. Error bars represent SEM. Unpaired *t* test: *P = 0.0225, 0.0172. **(G)** Cell proliferation measurement (WST-1 method) of *NADNMT1* DLD-1 cells treated as indicated. DAC: 2.5 μM. Dots indicate the mean of three independent replicates ($N = 3$), performed in technical triplicates ($n = 3$). Error bars represent SEM. # denotes $OD_{(450–690)} > 4$ indicating cell over confluency. Unpaired *t* test: ****P < 0.0001. Source data are available for this figure: SourceData FS4.

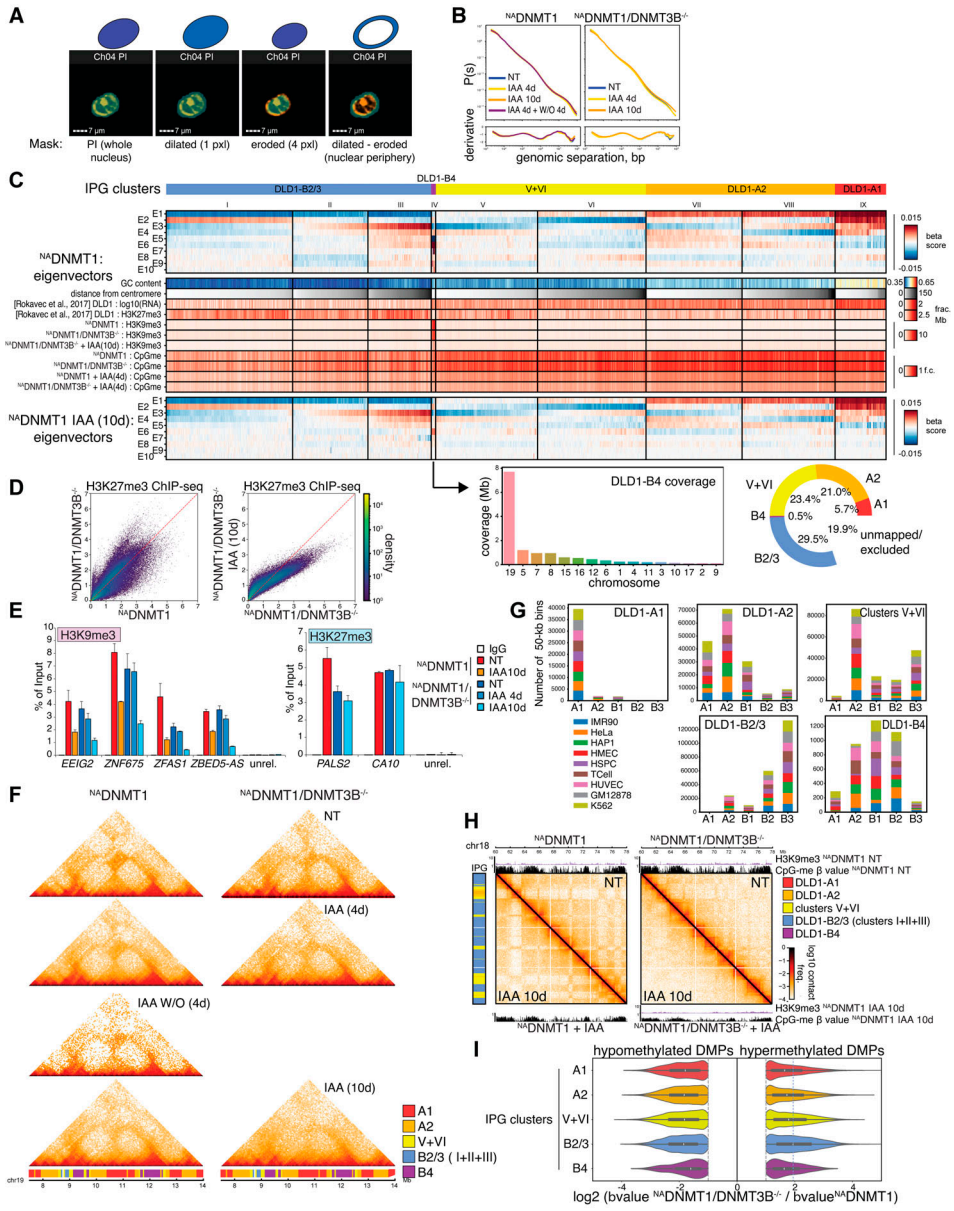

Figure S5. **Assignments of subnuclear compartmentalization of *NADNMT1* and *NADNMT1/DNMT3B*$^{-/-}$ DLD-1 cells. (A)** Representative ImageStream images and schematics showing mask building strategy for detection of nuclear and nuclear periphery areas. Masks are based on DNA area signal (PI). Dilated and eroded masks refer to pixels added (+1) and subtracted (−4) to the whole nuclear area, respectively. Pxl: pixel. Scale bar: 7 µm. **(B)** Plots showing interaction frequency as a function of genomic distance (P[s] curves) for Hi-C maps performed in the indicated cell lines and treatment conditions. Bottom panel shows the P(s) derivative indicating average size of extruded loops. W/O experiment was analyzed 4 days (d) after IAA withdrawal (IAA treatment: 4 days). **(C)** Integrated heatmaps of various features (rows) for each 50-kb genomic bin (column). Bins are sorted into groups derived from clustering of eigenvectors from untreated *NADNMT1* Hi-C data. Within each cluster, bins are sorted by distance from the centromere. Top section: consolidated IPG labels (color-coded) and eigenvector clusters labels I–IX below them, followed by the first 10 trans eigenvectors from untreated *NADNMT1* Hi-C. Middle section: Mean signal intensity of functional genomics features: GC content, distance from centromere, bulk RNA-seq signal and H3K27me3 ChIP-seq from WT DLD1 cells (Rokavec et al., 2017), H3K9me3 ChIP-seq, and CpG methylation data from this study. Bottom section: first 10 trans eigenvectors from 10-day IAA-treated *NADNMT1* Hi-C data, showing cluster IV (i.e., IPG DLD1-B4) as the most impacted by treatment. Bottom right inset: Donut plot of IPG composition across autosomes, showing 19% of regions excluded from analysis due to poor mapability or translocations. Bottom left inset: Distribution of DLD1-B4 coverage by chromosome shows it is predominantly found on chromosome 19. **(D)** Scatter plot showing H3K27me3 ChIP-seq signal density (mean fold change over input) upon DNMT3B deletion (left) and DNMT1 depletion (10 days, right) in *NADNMT1/DNMT3B*$^{-/-}$ cells. Each point represents a 10-kb genomic bin. **(E)** ChIP-qPCR analyses of H3K9me3 (left) and H3K27me3 (right) at selected genomic loci using the indicated primer sets (Table S1) as validation of relative ChIP-seq experiment in the shown cell lines and conditions. Error bars represent SEM. **(F)** Time courses of Hi-C in the chromosome 19 region from Fig. 4 E, in the indicated cell lines and conditions. W/O experiment was analyzed 4 days after IAA removal (IAA treatment: 4 days). **(G)** Distribution of SNIPER subcompartment label predictions of 50-kb loci from untreated *NADNMT1* cells, grouped by the de novo IPG classification in this study. **(H)** Example of DLD1-B2/3 interaction profile disruption of DLD1-B2/3 in the *NADNMT1/DNMT3B*$^{-/-}$ background compared with the *NADNMT1* one in a large region on chromosome 18. Relative H3K9me3 and CpG methylation (SWAN normalized β-value from the EPIC array) signals are also shown (as in Fig. 4 F). **(I)** Distribution of hypo and hypermethylated ($\log_2$ fold change < 2 and > 2, respectively) DMPs identified in *NADNMT1/DNMT3B*$^{-/-}$ cells compared to *NADNMT1* cells in the defined DLD-1 IPG clusters.

Provided online are Table S1 and Table S2. Table S1 lists the primers used in the work. Table S2 reports the number of significant differentially methylated probes identified between the experimental condition analyzed in this work.